Lymph node medulla regulates the spatiotemporal unfolding of resident dendritic cell networks

Milas Ugur, R. Jacob Labios, Chloe Fenton, Konrad Knöpper, Katarzyna Jobin, Fabian Imdahl, Gosia Golda, Kathrin Hoh, Anika Grafen, Tsuneyasu Kaisho, et al.

Article

Immunity

Lymph node medulla regulates the spatiotemporal unfolding of resident dendritic cell networks

Graphical abstract

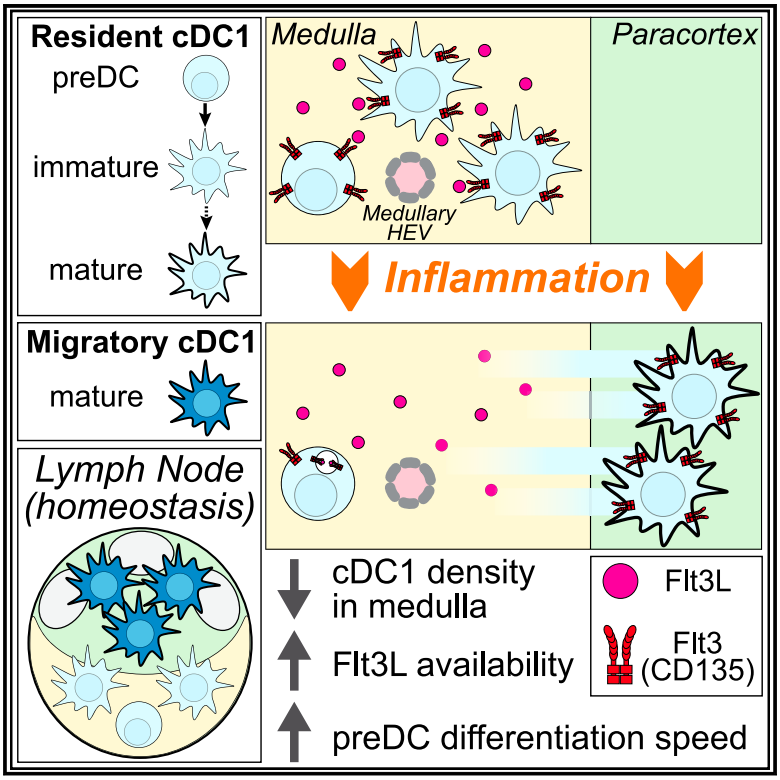

Authors

Milas Ugur, R. Jacob Labios, Chloe Fenton, ..., Georg Gasteiger, Marc Bajénoff, Wolfgang Kastenmüller

Correspondence

milas.ugur@uni-wuerzburg.de (M.U.), wolfgang.kastenmueller@uni-wuerzburg.de (W.K.)

In brief

Conventional dendritic cells (cDCs) are short-lived cells, being constantly replaced by precursors (preDCs) from the bone marrow. Ugur et al. provide insight into the niches that maintain these cells, showing that preDCs home to the LN medulla and generate a network that extends toward the paracortex. Inflammation promotes rapid maturation of cDC1s, leaving gaps in this network that are filled by local Flt3L feedback.

Highlights

- Resident and migratory cDC1s generate distinct networks in LNs
- The LN medulla is a niche for DC precursor homing and differentiation
- *Prtn3*-based fate tracking reveals differentiation trajectories of preDCs in LNs
- Local Flt3L-mediated feedback accelerates cDC1 development in the LN

Ugur et al., 2023, Immunity *56*, 1778–1793
August 8, 2023
https://doi.org/10.1016/j.immuni.2023.06.020

CellPress

CellPress
OPEN ACCESS

Immunity

Article

Lymph node medulla regulates the spatiotemporal unfolding of resident dendritic cell networks

Milas Ugur,[1,*] R. Jacob Labios,[1] Chloe Fenton,[1] Konrad Knöpper,[1] Katarzyna Jobin,[1] Fabian Imdahl,[2] Gosia Golda,[1] Kathrin Hoh,[1] Anika Grafen,[1] Tsuneyasu Kaisho,[3] Antoine-Emmanuel Saliba,[2] Dominic Grün,[1,2] Georg Gasteiger,[1] Marc Bajénoff,[4] and Wolfgang Kastenmüller[1,5,*]

[1]Würzburg Institute of Systems Immunology, Max Planck Research Group at the, Julius-Maximilians-Universität Würzburg, 97078, Würzburg, Germany

[2]Helmholtz Institute for RNA-Based Infection Research (HIRI), Helmholtz Centre for Infection Research (HZI), 97080 Würzburg, Germany

[3]Department of Immunology Institute of Advanced Medicine, Wakayama Medical University, 641-8509 Wakayama, Japan

[4]Aix Marseille Université, CNRS, INSERM, CIML, 13288 Marseille, France

[5]Lead contact

*Correspondence: milas.ugur@uni-wuerzburg.de (M.U.), wolfgang.kastenmueller@uni-wuerzburg.de (W.K.)

https://doi.org/10.1016/j.immuni.2023.06.020

SUMMARY

Unlike macrophage networks composed of long-lived tissue-resident cells within specific niches, conventional dendritic cells (cDCs) that generate a 3D network in lymph nodes (LNs) are short lived and continuously replaced by DC precursors (preDCs) from the bone marrow (BM). Here, we examined whether specific anatomical niches exist within which preDCs differentiate toward immature cDCs. *In situ* photoconversion and *Prtn3*-based fate-tracking revealed that the LN medullary cords are preferential entry sites for preDCs, serving as specific differentiation niches. Repopulation and fate-tracking approaches demonstrated that the cDC1 network unfolded from the medulla along the vascular tree toward the paracortex. During inflammation, collective maturation and migration of resident cDC1s to the paracortex created discontinuity in the medullary cDC1 network and temporarily impaired responsiveness. The decrease in local cDC1 density resulted in higher Flt3L availability in the medullary niche, which accelerated cDC1 development to restore the network. Thus, the spatiotemporal development of the cDC1 network is locally regulated in dedicated LN niches via sensing of cDC1 densities.

INTRODUCTION

Conventional dendritic cells (cDCs) are mononuclear phagocytes that are equipped with a plethora of innate immune sensors, allowing them to constantly probe and respond to changes in their microenvironment. With their capacity to relay this information to T cells, they form an essential bridge between the innate and adaptive immune system.[1] Based on this capacity, cDCs can both promote and dampen immune responses, making them key targets to treat diverse diseases, ranging from autoimmunity to infection and cancer.[2,3] There are two major subsets of cDCs: cDC1, which specializes in activating $CD8^+$ T cells, and cDC2, whose predominant feature is to stimulate $CD4^+$ T cells.[4,5] During homeostasis, both subsets develop from dedicated precursors (preDCs) that exit the bone marrow (BM) and continuously seed tissues.[6,7]

In the tissue, cDCs form distinct cellular networks and undergo a process of homeostatic maturation, which is reflected by increased expression of major histocompatibility complex class II (MHCII) and the chemokine receptor CCR7. In draining lymph nodes (dLNs), migratory cDC1s and cDC2s coalesce with distinct populations of LN-resident cDC1s and cDC2s, which reach the LN as preDCs via the blood and remain within LNs in homeostasis and during inflammation. Together, these four cDC populations form a complex network that is further reorganized upon inflammation. Despite significant advances in multicolor imaging, the highly complex 3D network of cDCs in LNs, which is composed of various subsets and activation states, is incompletely understood.[8–10] How the cDC networks are generated and maintained is conceptually interesting given the continuous migration and short lifespan of its cellular elements.[11] This is in stark contrast to the extensively studied macrophage networks, which are composed of long-lived tissue resident cells that settle within specific niches.[12]

The key question is whether specific anatomical niches exist within which preDCs differentiate toward immature cDCs, and if so, which factors regulate this development. The current view is that preDCs enter the LN via paracortical high endothelial venules (HEVs), randomly integrate into the network and develop into immature cDCs—a model that does not involve topographic niches.[13–15] Therefore, we set out to address whether specific niches in LNs exist in which preDCs develop into immature DCs and how these cells generate and maintain a three-dimensional network.

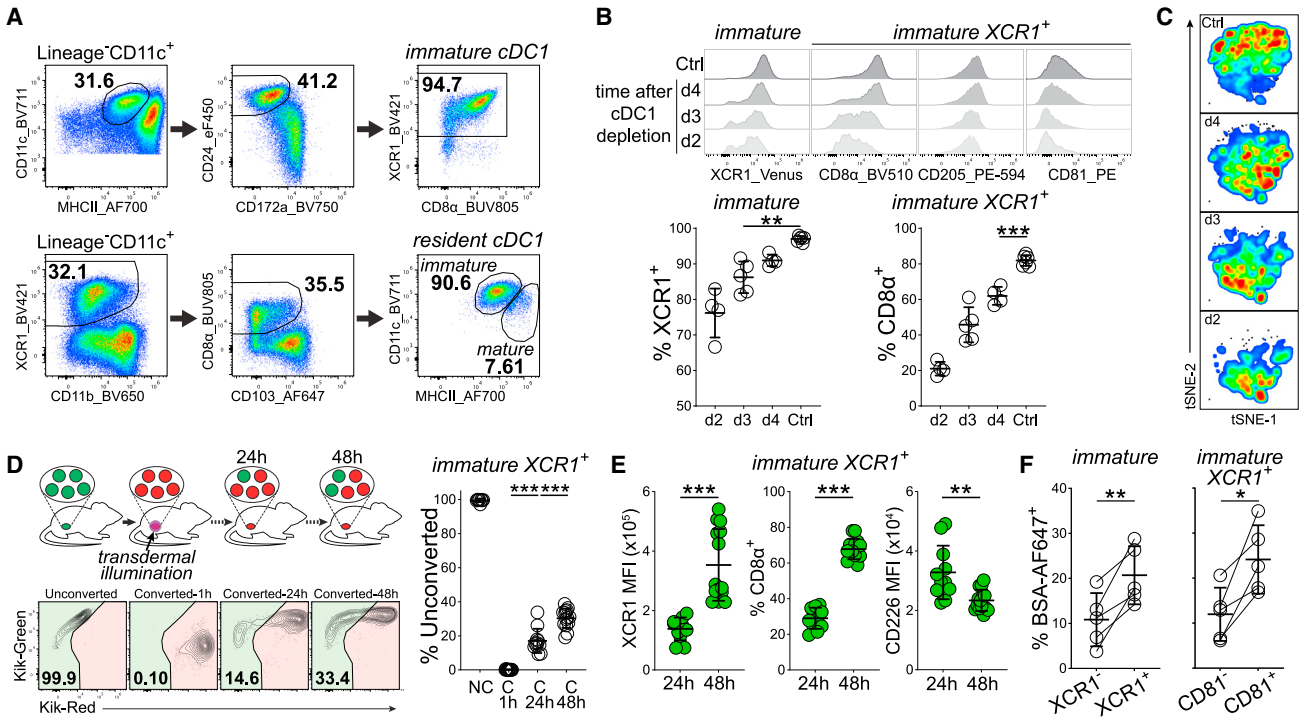

Figure 1. Fully functional resident cDC1s gradually develop from preDCs over several days

(A) Representative gating strategies for cDC1s in LNs of WT mice. MHCII^{lo}CD24^{+} gate shows immature cDC1s (top) and XCR1^{+}CD8α^{+} gate shows resident cDC1s (immature and mature) (bottom).

(B and C) Analysis of immature cDC1 (MHCII^{lo}CD24^{+}) repopulation in LNs of *Xcr1*^{DTR} mice 2, 3, or 4 days after cDC1 depletion. Expression levels of XCR1-Venus reporter, CD8α, CD205, and CD81 (B) and multidimensional tSNE analysis of flow cytometric data using 13 markers (C).

(D and E) Analysis of newly developing unconverted (K-Red^{-}K-Green^{+}) immature cDC1s (MHCII^{lo}CD24^{+}XCR1^{+}) after transdermal photoconversion of inguinal LNs in *Xcr1*^{KikGR} mice. Frequency of unconverted (K-Red^{-}K-Green^{+}) cells among immature cDC1s (MHCII^{lo}CD24^{+}XCR1^{+}) (D) and expression levels of XCR1, CD8α, and CD226 among unconverted (K-Red^{-}K-Green^{+}) immature cDC1s (MHCII^{lo}CD24^{+}XCR1^{+}) (E).

(F) Analysis of antigen uptake by immature cDC1s (MHCII^{lo}CD24^{+}) in draining LNs of WT mice 2 h after s.c. injection of BSA-AF647 (bovine serum albumin) into the foot hock. Frequency of BSA-AF647^{+} cells among XCR1^{-} vs. XCR1^{+} (left) and CD81^{-} vs. CD81^{+} cells (right).

Data display one representative of ≥2 independent experiments (A and C) or pooled data from ≥2 independent experiments (B and D–F) (A, n ≥ 3; B and C, n = 4–6; D and E, n = 4–7 using 8–14 LNs; F, n = 5). Error bars indicate the mean ± SD. Comparison between groups was calculated using one-way ANOVA, paired or unpaired Student's t tests. ***p value < 0.001, **p value < 0.01, *p value < 0.05.

By combining analysis of a novel cDC genetic fate-tracking model, depletion-repopulation kinetics, *in situ* labeling, single-cell RNA sequencing (scRNA-seq), preDC transfer, and *in vivo* imaging, we found that preDCs are predominantly recruited to the LN medulla, where they undergo several lineage-specific developmental steps that precede their homeostatic maturation. Furthermore, our analyses showed that the preDC exposure to Flt3L within the medullary niche depends on the local density of immature cDC1s. This, in turn, affects the speed of cDC1 development within the medullary niche. Taken together, our data demonstrate that cDC1 development in LNs occurs within a specific microanatomical niche. This niche controls the spatio-temporal unfolding of a dynamic cDC1 network in a conveyor belt-like sequence that begins in the medulla and extends to the paracortex.

RESULTS

Gradual development of LN-resident immature cDC1s

To study the spatiotemporal development of cDCs, we first focused on cDC1. In LNs, we identified immature cDC1s based on MHCII^{lo} and CD24^{+} staining, which are resident and mostly XCR1^{+} (Figures 1A and S1A–S1C).[16] Some resident cDC1s also mature in LNs and can be distinguished from migratory cDC1s based on CD8α and CD103 expression, regardless of their maturation state. Migratory cDC1s were CD8α^{-}CD103^{+} and functionally in a mature state, reflected by high MHCII and CCR7 expression (Figures 1A and S1A–S1D). By contrast, resident cDC1s expressed CD8α and were predominantly in an immature state, indicated by low MHCII and CCR7 levels (Figures 1A and S1A–S1D).

To synchronize cDC1 development, we systemically depleted cDC1s in *Xcr1*^{DTR} mice and analyzed immature cDC1s during their repopulation in LNs. As previously suggested, we detected a stepwise increase of several surface molecules, such as XCR1, CD8α, CD205, and CD81, *in vivo* that required about 4 days to reach similar levels as in non-depleted controls (Figures 1B and S1E).[17] t-distributed stochastic neighbor embedding (t-SNE) analysis of 13 markers to plot our multiparameter fluorescence-activated cell sorting (FACS) data showed a continuous development of immature cDC1 (Figure 1C). Importantly, immature cDC1s did not equally distribute along this developmental

path at steady state but enriched at late developmental stages (Figures 1B and 1C).

Next, we wished to validate the relatively long repopulation kinetic of cDC1s in non-depleted conditions and therefore used an *in situ* labeling approach with *Xcr1*^{KikGR} mice. Upon illumination, KikGR can be converted from a green-fluorescent to a red-fluorescent state. Importantly, we were able to completely photoconvert all cDC1s in inguinal LNs through the skin without surgical intervention (Figure 1D). Thereby, we could discriminate newly developing immature cDC1s (unconverted, Kik-Green^{+}Kik-Red^{-}) from older photoconverted Kik-Red^{+} cDC1s when analyzing these LNs after photoconversion via flow cytometry (Figure 1D). By 24 h, about 15%, and by 48 h, about 30% of immature cDC1s were unconverted. These newly developing cDC1s showed a significant increase of XCR1 and CD8α expression from 24 to 48 h, whereas CD226 expression, a marker for cDC1-dedicated preDCs, was reduced (Figures 1E and S1F).[18] Functionally, the uptake capacity of fluorescently labeled protein *in vivo* by immature cDC1s improved as they developed and correlated with the expression levels of XCR1 and CD81 (Figure 1F). Together, these results established that immature cDC1s gradually develop from preDCs over several days and accumulate to a fully functional state at a population level.

A *Prtn3*-based mouse model to fate-track cDC precursors

In order to gain in-depth insights on the gradual development of resident cDCs, including cDC2s, an ideal mouse model should be able to track the development of a single wave of preDCs in an unperturbed environment. Analysis of available datasets (Immgen.org) revealed a broad expression of *Prtn3* in BM progenitors, including common DC precursors. Importantly, *Prtn3* expression was absent in cDCs in blood and LNs (Figure S2A). Therefore, we generated transgenic mice in which we inserted a Cre-ERT2 and a human CD4 (hCD4) cassette at the 3′ end of the endogenous *Prtn3* gene, separated by internal ribosome entry site (IRES) elements (Figure S2B). Flow cytometric analysis of BM and LN cells of these mice showed an hCD4 expression pattern that matched the transcriptomic analysis arguing for faithful expression of the inserted cassette (Figures 2A and S2A). For fate-tracking of *Prtn3*-expressing cells we crossed these mice to *Rosa26*$^{LSL\text{-}tdTomato}$ mice (hereafter *Prtn3*$^{LSL\text{-}Tom}$) (Figure 2B). Following tamoxifen treatment (24 h) of *Prtn3*$^{LSL\text{-}Tom}$ mice, we readily observed Tomato expression in BM cells that was consistent with the hCD4 expression pattern (Figures 2C, S2C, and S2D). Using this approach, we labeled about 30% of common dendritic cell progenitors (CDPs), whereas the highest frequency (about 70%) of Tomato^{+} cells was observed in granulocyte-monocyte progenitors (GMPs), granulocyte progenitors (GPs), and common monocyte progenitors (cMoPs) (Figures 2C, S2C, and S2D). At this time point, we did not detect Tomato labeling in LNs except for a small population of Ly6C^{hi} monocytes, indicating that DCs are not locally labeled (Figure 2C). Next, following a single injection of tamoxifen, we analyzed the frequency of Tomato-labeled cells among precursor populations in the BM over 7 days. The highest frequencies of Tomato^{+} cells were detected at day 3 and then sharply declined by day 7 post-tamoxifen treatment (Figure 2D). Therefore, tamoxifen treatment of *Prtn3*$^{LSL\text{-}Tom}$ mice led to a pulsed labeling of a wave of myeloid precursor cells that included progenitors of granulocytes, monocytes, and cDCs, allowing for the analysis of their fate over time. We next wanted to elucidate the developmental stages of cDCs in LNs. After a single dose of tamoxifen, we observed a gradual loss of labeled preDCs (CD11c^{+}MHCII^{-}) from day 3 to day 7, whereas the fraction of labeled mature cDCs (MHCII^{hi}) increased over time (Figure 2E). Therefore, *Prtn3*$^{LSL\text{-}Tom}$ mice allow for a kinetic analysis of cDC development in LNs during homeostasis. Next, we specifically analyzed resident cDC1s (MHCII^{lo}CD24^{+}) and observed a gradual upregulation of both XCR1 and CD8α over time, consistent with our prior results (Figure S2E). Together, we have established a new mouse model to track the fate of BM progenitor cells, including CDP.

LN preDCs are lineage committed and undergo distinct developmental paths

To study the early steps of preDC differentiation in the LN, we treated *Prtn3*$^{LSL\text{-}Tom}$ mice with tamoxifen and sorted Tomato^{+} preDCs (CD11c^{+}MHCII^{-}CD135^{+}) 3, 5, and 7 days later and mixed them with preDCs from wild-type (WT) mice for comparative scRNA-seq (Figures 2F and S2F). Uniform manifold approximation and projection (UMAP)-based clustering of the combined datasets showed 10 different clusters (Figures 2G–2I). Cluster 5 expressed highest levels of genes that were previously associated with CDP in the BM[19] and therefore included the earliest stages of preDCs that entered the LN (Figures 2G and S2G). Separate analysis of this cluster revealed an additional heterogeneity within this population (Figure S2H). Specifically, we detected four populations that represented preDC1 and three clusters of preDC2 with a differential expression pattern of *Irf8, Irf4, Batf3, Zeb2, Tcf4*, and *Klf4* (Figure S2H; Table S1). Therefore, preDC2s appeared to be heterogeneous and likely comprise further developmentally biased differentiation states in contrast with preDC1s. Next, we set cluster 5 as a starting point to infer a lineage trajectory of cDC development using a slingshot analysis (Figure 2G). The developmental path of preDC2s appeared to be highly complex and consisted of seven clusters and three distinct developmental trajectories (Figure 2G). One trajectory represented the development into early *bona fide* cDC2s, projected onto cluster 8, and was characterized by the expression of *Sirpa*, *Esam*, and *Clec4a2* (Figures 2G–2I). A second trajectory projected onto cluster 0, which lacked *Zbtb46* but expressed genes that are typically associated with plasmacytoid DCs (pDCs), such as *Siglech*, *Ly6d*, and *Il7r* (Figures 2G–2I). The third trajectory toward cluster 4 was characterized by the expression of *Irf4* and *Cx3cr1* (Figures 2G–2I). This population resembled previously identified transitional DCs with features of both pDCs and cDC2s.[20] Together, these data suggest that preDC2 development is highly plastic within LNs, allowing for additional fates besides *bona fide* cDC2s, such as pDCs and transitional DCs. By contrast, the development of cDC1s appeared to follow a straight developmental line from preDC1s via cluster 2 to cluster 9. The cells along this trajectory homogeneously expressed *Cd24a* and *Batf3*, supporting its association with the cDC1 lineage (Figures 2G–2I). We further observed an increase of *Xcr1, CD8*α, and *Cd81* expression along the "pseudo-time" of cDC1 development (Figure S2I). By contrast, *Cd226* expression decreased along this trajectory in accordance with our previous results. Flow cytometric analysis of preDCs (CD11c^{+}/MHCII^{-}/CD135^{+}) confirmed the heterogeneous

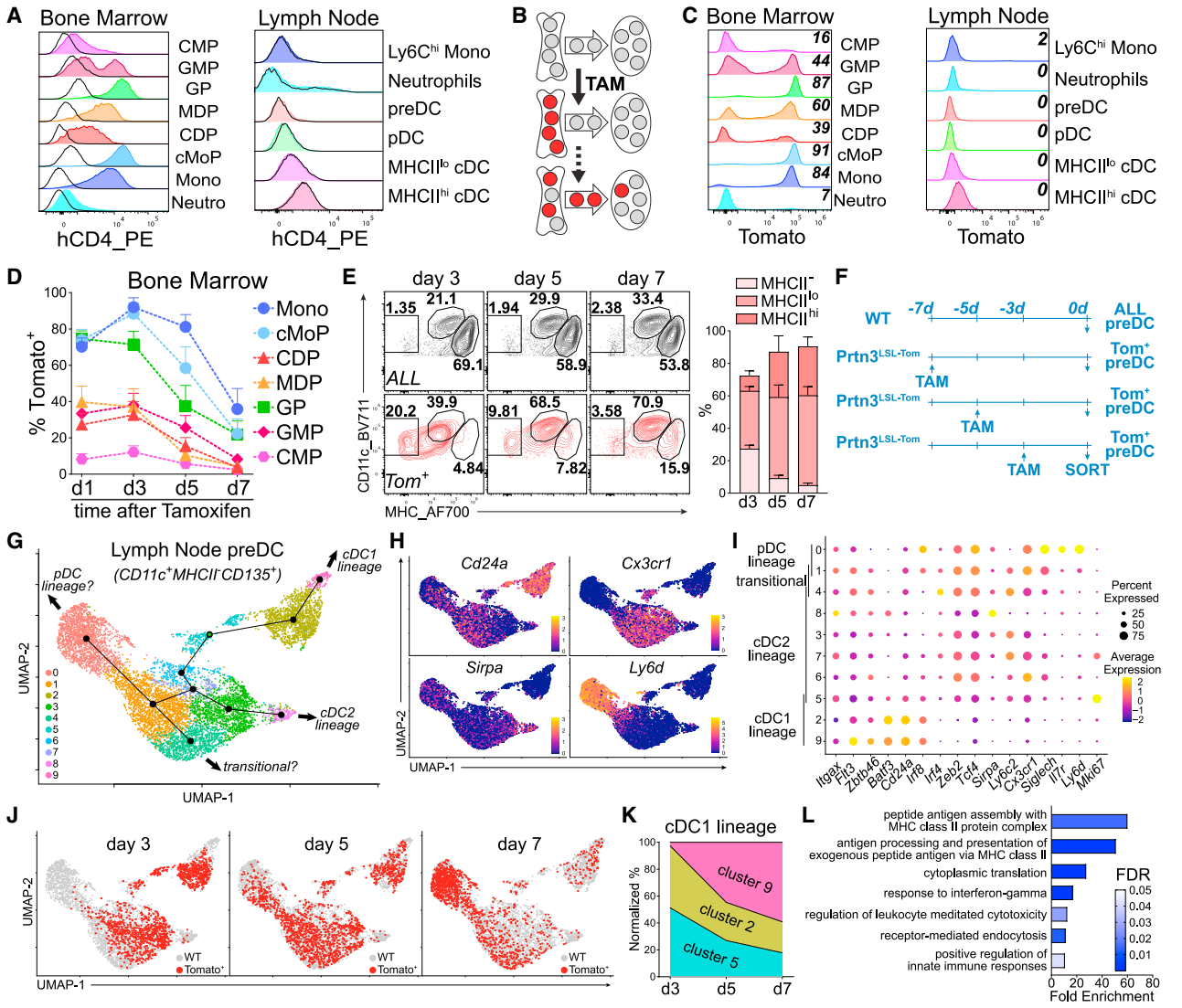

Figure 2. *Prtn3*-based fate-tracking reveals early phases of DC development in LNs

(A) Expression of the human CD4 reporter among the indicated populations in the BM and LNs of *Prtn3*$^{CreERT2\text{-}hCD4}$ mice. Black lines show WT controls. CMP, common myeloid progenitor; GMP, granulocyte-monocyte progenitor; GP, granulocyte progenitor; MDP, monocyte-dendritic cell progenitor; cMoP, common monocyte progenitor; Mono, monocytes; Neutro, neutrophils; pDC, plasmacytoid dendritic cell.

(B) Diagram showing the labeling/fate-tracking of a wave of myeloid precursors in the BM of *Prtn3*$^{LSL\text{-}Tom}$ mice after tamoxifen injection and the consequent migration to LNs.

(C) Frequency of Tomato$^+$ cells among the indicated populations in the BM and LNs of *Prtn3*$^{LSL\text{-}Tom}$ mice 24 h after tamoxifen injection.

(D) Frequency of Tomato$^+$ cells among the indicated populations in the BM of *Prtn3*$^{LSL\text{-}Tom}$ mice 1, 3, 5, and 7 days after tamoxifen injection.

(E) Frequency of MHCII$^-$, MHCII^{lo}, and MHCII^{hi} cells among all (top) or Tomato$^+$ (bottom) cDCs (Lin$^-$(Ly6C^{hi}CD11b$^+$)$^-$B220$^-$CD11c$^+$) in LNs of *Prtn3*$^{LSL\text{-}Tom}$ mice 3, 5, and 7 days after tamoxifen injection.

(F–L) Single-cell RNA sequencing (scRNA-seq) analysis of preDCs in LNs.

(F) Experimental setup. PreDCs (CD11c$^+$MHCII$^-$CD135$^+$) from LNs of unmanipulated WT mice and Tomato$^+$ preDCs from LNs of *Prtn3*$^{LSL\text{-}Tom}$ mice that received tamoxifen injection 3, 5, or 7 days earlier were sorted and analyzed by scRNA-seq.

(G) Uniform manifold approximation and projection (UMAP) plot displaying 8,516 scRNA-seq transcriptomes clustered in 10 different clusters. Lines indicate different lineage trajectories calculated by the Slingshot algorithm starting from cluster 5.

(H) UMAP plots displaying expression of *Cd24a*, *Cx3cr1*, *Sirpa*, and *Ly6d* genes.

(I) Dotplot of representative marker genes associated with the identified clusters. Color indicates the *Z* score mean of the expression values across clusters and dot size represents fraction of cells in the cluster expressing the respective genes.

(J) UMAP plot showing the distribution of Tomato$^+$ preDCs among the clusters 3, 5, or 7 days after tamoxifen injection.

(K) Normalized percentages of Tomato$^+$ cells within the cDC1 lineage associated clusters (5, 2, and 9) 3, 5, or 7 days after tamoxifen injections.

(L) Gene ontology terms enriched among genes that are upregulated during the early development of the cDC1 lineage in LNs. FDR, false discovery rate.

Data display one representative of ≥2 independent experiments (A–D), pooled data from ≥2 independent experiments (E) or data from 1 experiment (F–L) (A, C, and D, n = 4; E, n = 6). Error bars indicate the mean ± SEM.

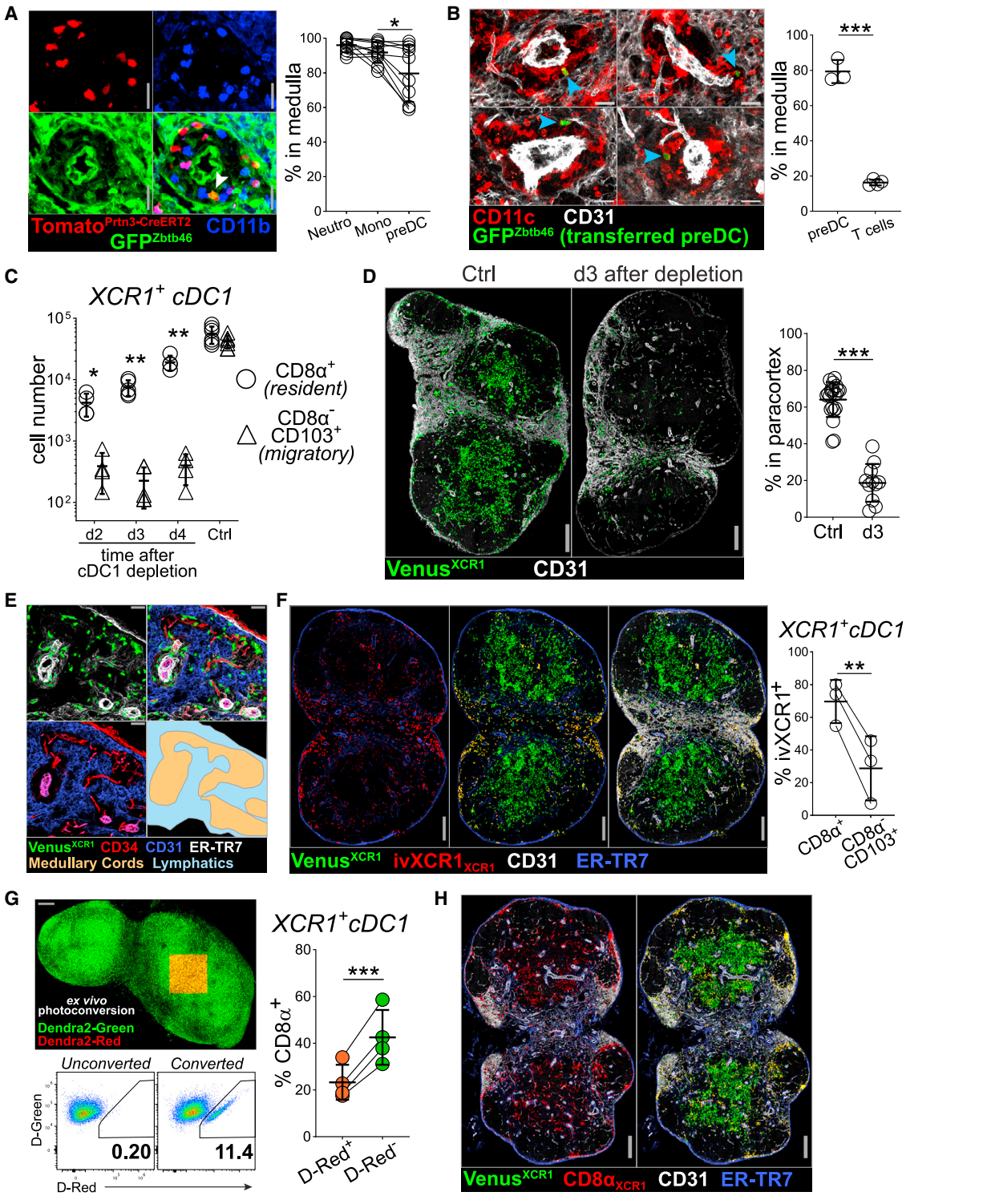

Figure 3. preDCs enter via medullary HEVs and develop in the LN medulla

(A) Confocal microscopy showing Tomato$^+$ monocytes, neutrophils, and cDCs in LNs of *Prtn3*$^{LSL\text{-}Tom}$*Zbtb46*^{GFP} mice 3 days after tamoxifen injection. Arrow shows a Tomato$^+$GFP$^+$ preDC in a medullary cord (left). Frequency of cells in medulla among monocytes, neutrophils, and cDCs (right).

(B) Confocal microscopy showing GFP$^+$ preDCs in LNs of WT mice 2 h after i.v. transfer of preDCs from the BM of *Zbtb46*^{GFP} mice (left). Arrows show GFP$^+$ preDCs in medullary cords (left). Frequency of cells in medulla among transferred preDCs and transferred T cells 2 h after i.v. transfer into WT (right).

(C) Cell numbers of resident (CD8α^+) or migratory (CD8α^-CD103$^+$) XCR1$^+$ cDC1s in 6 LNs of *Xcr1*^{DTR} mice at indicated time points after depletion of cDC1s with DTx injection.

(legend continued on next page)

expression of CD24, CX3CR1, Ly6C, CD117, CD8α, and XCR1 on a protein level, consistent with our scRNA-seq data (Figure S2J). To support the bioinformatically inferred developmental path of preDCs, we separated the combined datasets based on the timing of tamoxifen-induced Tomato labeling (*Prtn3*$^{LSL\text{-}Tom}$) (Figure 2J). Next, we quantified the relative abundance of Tomato$^+$ cells along the cDC1 trajectory from cluster 5 via cluster 2 to cluster 9 (Figure 2K). This "real-time" developmental trajectory confirmed the computational pseudo-time analysis inferred above. Gene ontology enrichment analysis of our scRNA-seq data showed that cDC1 development was associated with the upregulation of pathways that are critical for cDC1 function, including antigen presentation and innate immune activation (Figure 2L). Taken together, these data revealed the continuous, temporal development of preDCs into various subsets and states.

preDCs home and develop in the medulla and generate a distinct network of resident cDC1s

Next, to identify dedicated spatial niches of cDC development, we crossed *Prtn3*$^{LSL\text{-}Tom}$ with *Zbtb46*^{GFP} mice allowing us to unambiguously identify developing cDCs on LN sections. 3 days after tamoxifen treatment, ~80% of early developing cDCs (Tomato$^+$/GFP$^+$) were localized in the LN medulla, outside the paracortex, together with other Tomato$^+$ myeloid cells, such as neutrophils and monocytes (Figures 3A and S3A). To further investigate this finding, we transferred sorted preDCs from the BM of *Zbtb46*^{GFP} mice and analyzed their location in LNs 2 h later. Systematic quantitative analyses of ~450 LN sections showed that the dominant entry site of preDCs is the LN medulla, in contrast to T cells that primarily enter LNs via paracortical HEVs and localize to the paracortex 2 h post-transfer (Figures 3B, S3B, and S3C). CD62L blockade (2 days) had a partial effect on preDC numbers, whereas it significantly reduced T cell abundance in LNs (Figure S3D). Further microscopic analysis suggested that preDCs enter mostly via medullary HEVs (order I/II) (Figure S3E). These results suggested that preDCs, besides medullary HEVs, might also extravasate via regular medullary venules and/or utilize additional molecular pathways for extravasation, although CD62E/P or Sphingosine-1-phosphate did not seem to be involved (Figure S3F and S3G). Next, we took advantage of the different repopulation kinetics of resident vs. migratory cDC1s in the LN following systemic depletion using *Xcr1*$^{DTR/Venus}$ mice. Quantitative FACS-based analysis showed that in contrast to resident (CD8α$^+$) cDC1s, migratory (CD8α$^-$CD103$^+$) cDC1s had not significantly repopulated the LN in the first 4 days post-depletion (Figure 3C). Confocal analysis of LN sections from non-depleted control mice showed a mixed localization of cDC1s in the paracortex and medulla (Figures 3D and S3H). Following depletion, cDC1s predominantly repopulated the LN at the medullary zone and were sparse in the paracortex (Figures 3D and S3H). Detailed analysis revealed that resident XCR1$^+$ cDC1s were developing in medullary cords and accumulated around medullary blood vessels confirming our fate-tracking results (Figure 3E). These data further suggested that resident and migratory cDC1s generate distinct, spatially segregated networks. To test this, we made use of the preferential localization of resident cDC1s around blood vessels: injected labeled αXCR1 antibody i.v., harvested and analyzed the LNs 1 h later. This time frame allows the antibody to penetrate the tissue around blood vessels, yet not deeply into the LN parenchyma that is the paracortex. As expected, αXCR1 antibody exclusively labeled cDC1s close to blood vessels, particularly in the medulla (Figure 3F). FACS analysis of LNs from the same mice showed that i.v. αXCR1-antibody labeled cDC1s were predominantly LN-resident cDC1s (Figure 3F). Next, we generated thick (200 μm) vibratome sections of LNs from photoconvertible Dendra2 transgenic mice and photoconverted an area within the paracortex of the LN (Figure 3G). Subsequent flow cytometry analysis of photoconverted cDC1s showed a significant underrepresentation of LN-resident cDC1s, indicating that they are sparse in the paracortex (Figure 3G). Finally, we made use of the selective expression of CD8α in LN-resident cDC1s. Because CD8α is also prominently expressed on CD8 T cells, we depleted CD8 T cells in cDC1 reporter mice (*Xcr1*^{Venus}) using CD8β-specific depleting antibodies. This approach allowed us to distinguish XCR1$^+$CD8α$^+$ resident from XCR1$^+$CD8α$^-$ migratory cDC1s using CD8α staining on LN sections. Although migratory cDC1s were largely found in the paracortex, resident cDC1 predominantly populated the medulla and cortical lymphatic sinuses that enclosed adjacent B cell follicles (Figure 3H). Together, these results established that the LN medulla is the prime site of preDC homing and provides a niche for local cDC development. Additionally, we demonstrated that immature LN-resident cDC1s form a distinct three-dimensional (3D) network that is associated with blood vessels and spatially separated from migratory cDC1s that populate the paracortex. Next, we wished to elucidate how this network unfolds spatially.

Conveyor-belt-like progression of the cDC1 network from the LN medulla

The entry route of preDCs begged the question how developing immature cDCs navigate through the LN to reach the T cell

(D) Confocal microscopy showing XCR1$^+$ cDC1s in LNs of non-depleted control and 3 days after depletion of cDC1s with DTx injection in *Xcr1*$^{DTR/Venus}$ mice. Representative images (left). Frequency of cells in paracortex among XCR1$^+$ cDC1s (right).
(E) Localization of XCR1$^+$ cDC1s in medullary cords within the medulla in LNs of *Xcr1*^{Venus} mice.
(F) Analysis of LNs of *Xcr1*^{Venus} mice 1 h after i.v. injection of anti-XCR1 antibody. Confocal microscopy showing i.v.-labeled cDC1s (left) and flow cytometric analysis showing percentages of i.v.-labeled cells among resident (CD8α$^+$) or migratory (CD8α$^-$CD103$^+$) XCR1$^+$ cDC1s (right).
(G) *Ex vivo* photoconversion of the paracortex of LN slices from Dendra2 mice and the subsequent analysis of these photoconverted LN slices via flow cytometry. Representative image after photoconversion (left top), flow cytometric analysis showing frequency of D-Red$^+$ converted cells among XCR1$^+$ cDC1s (left bottom) and percentage of CD8α$^+$ cells among D-Red$^+$ or D-Red$^-$ XCR1$^+$ cDC1s (right).
(H) Confocal microscopy showing CD8α$^+$ XCR1$^+$ cDC1s in LN of *Xcr1*^{Venus} mice after depletion of CD8β$^+$ cells with antibody injection.
Images are representative of ≥2 independent experiments (A, B, and D–H) and data display pooled data from ≥2 independent experiments (A–D, F, and G) (A, n = 5 using 2 LNs/n; B, n = 3–4 using 1–6 LNs/n; C, n = 4–6; D, n = 4–8 using 1–4 LNs/n; E, n ≥ 3; F, n = 3 using 1–2 LNs/n; G, n = 4 using 2–4 LNs/n; H, n = 3 using 1–3 LNs/n). Error bars indicate the mean ± SD. Comparison between groups was calculated using one-way ANOVA, paired or unpaired Student's t tests. ***p value < 0.001, **p value < 0.01, *p value < 0.05. Scale bars: 20 μm in (A) and (B); 30 μm in (E); and 200 μm in (D) and (F)–(H).

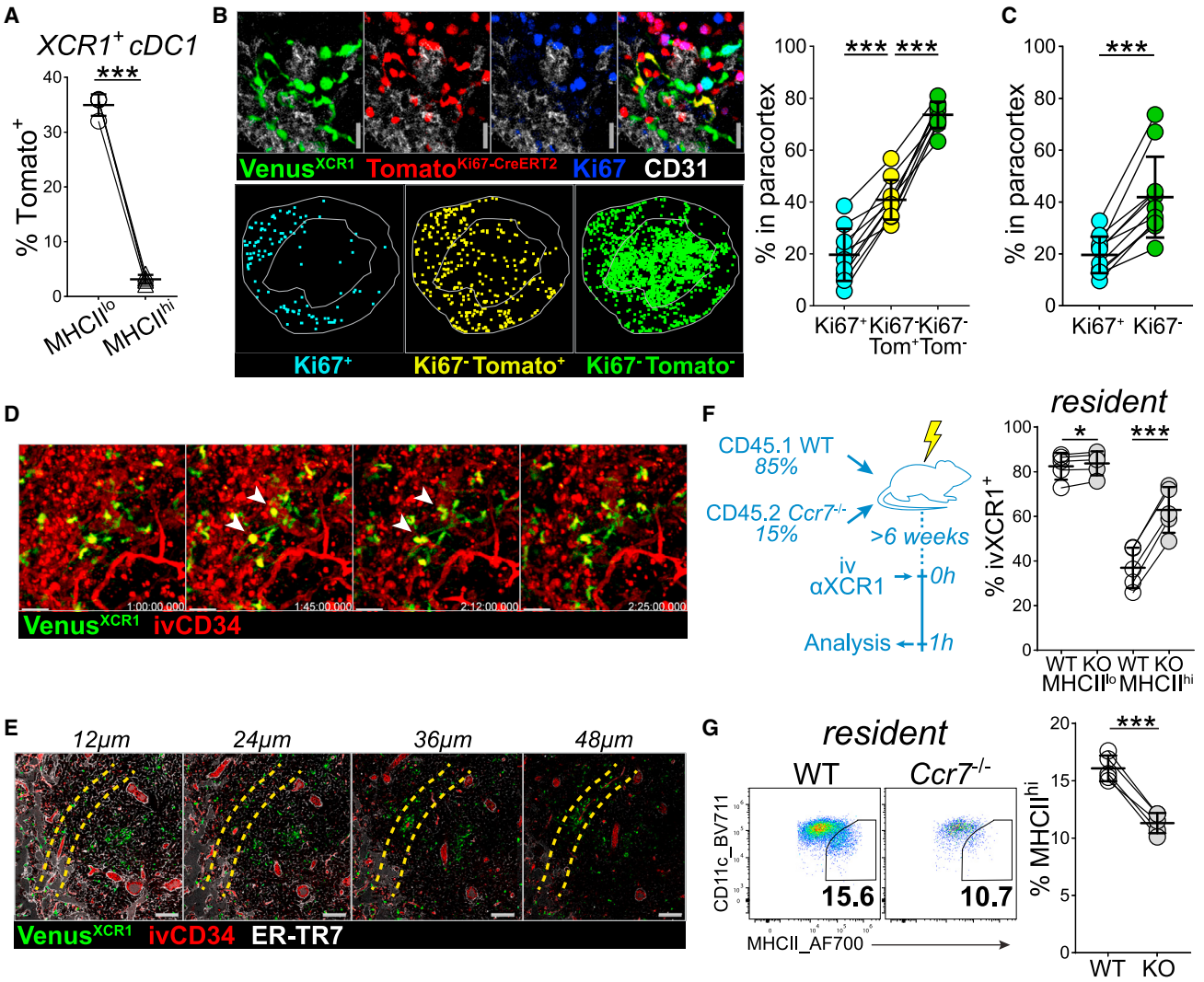

Figure 4. Resident cDC1s migrate from medulla toward paracortex during their development

(A) Frequency of Tomato$^+$ cells among MHCII^{lo} or MHCII^{hi} XCR1$^+$ cDC1s from LNs of *Mki67*$^{LSL\text{-}Tom}$ mice treated with tamoxifen 40 h before sacrifice.

(B) Localization of XCR1$^+$ cDC1s in LNs of *Mki67*$^{LSL\text{-}Tom}$*Xcr1*^{Venus} mice treated with tamoxifen 40 h before sacrifice. Confocal microscopy (left top), localization of the indicated XCR1$^+$ cDC1 populations in a representative LN (left bottom, outer gray line outlines the LN border and inner gray line outlines the paracortex) and frequency of cells in the paracortex among the indicated populations.

(C) Frequency of cells in the paracortex among Ki67$^+$ or Ki67$^-$ XCR1$^+$ cDC1s in LNs of *Xcr1*$^{DTR/Venus}$ mice 3 days after depletion of cDC1s with DTx injection.

(D) Intravital microscopy images showing local proliferation of XCR1$^+$ cDC1s in the LN medulla of *Xcr1*$^{DTR/Venus}$ mice 68 h after depletion of cDC1s with DTx. White arrows show proliferating cDC1s in medulla.

(E) Confocal microscopy of vibratome slices XCR1$^+$ cDC1s around blood vessels in LNs of *Xcr1*$^{DTR/Venus}$ mice 3 days after depletion. Yellow lines outline a vessel extending from medulla to paracortex and images show the same spot at different depth/z stack.

(F and G) Mixed WT:*Ccr7*$^{-/-}$ (85:15) BM chimeras were injected i.v. αXCR1 antibody 1 h before sacrifice (n = 5 mice in 2 experiments). Experimental setup (left) and frequency of ivXCR1$^+$ cells among WT or *Ccr7*$^{-/-}$ (KO) cells for MHCII^{lo} and MHCII^{hi} cells in resident (XCR1$^+$CD8α$^+$) cDC1s (right) (F). Frequency of MHCII^{hi} cells among WT or *Ccr7*$^{-/-}$ (KO) resident (XCR1$^+$CD8α$^+$) cDC1s (G).

Images are representative of ≥2 independent experiments (B, D, and E) and data display pooled data from ≥2 independent experiments (A–C, F, and G) (A, n = 4; B, n = 3 using 3–4 LNs/n; C, n = 3 using 3–4 LNs/n; D, n = 4 using 1–2 LNs/n; E, n = 3 using 1–3 LNs/n; F and G, n = 5). Error bars indicate the mean ± SD. Comparison between groups was calculated using one-way ANOVA or paired Student's t tests. ***p value < 0.001, *p value < 0.05. Scale bars: 20 μm in (B); 30 μm in (D); and 100 μm in (E).

areas where they ultimately execute their function. Because preDCs selectively expressed high levels of the proliferation associated gene *Mki67*,[15,21] we crossed *Mki67*^{CreERT2} mice with *Rosa26*$^{LSL\text{-}tdTomato}$ and with *Xcr1*^{Venus} mice. Upon tamoxifen treatment, Tomato$^+$ cDC1 were readily detectable 40 h later and were in an immature state (Figure 4A). In combination with Ki67 staining, we were able discern three distinct populations in LN sections: (1) Ki67$^+$ cDC1s that are currently proliferating, (2) Tomato$^+$Ki67$^-$ cells that recently proliferated, and (3) double-negative cDC1s that did not proliferate during or after

tamoxifen treatment (Figure 4B). When mapping these three populations, we found that actively proliferating cells were localized in the LN medulla, whereas cDC1s that had proliferated previously were partly localized in the paracortex, and non-proliferating cDC1s were primarily found in the paracortex (Figure 4B). This suggested that developing immature cDC1s move from the medulla toward the adjacent paracortex before maturation. To synchronize cDC1 development and to exclude migratory cDC1s from our analysis, we resorted to our depletion/repopulation approach and stained for Ki67 on cDC1s 3 days after depletion. In line with our previous results, we detected Ki67 expressing cDC1s primarily in the LN medulla, whereas Ki67-negative cDC1s were enriched in the T cell zone (Figure 4C). This experimental approach allowed us to directly observe cDC1 proliferation *in vivo* using intravital 2-photon microscopy. When imaging the LN medulla of *Xcr1*$^{DTR/Venus}$ mice 3 days after diphtheria toxin (DTx) treatment, we readily observed numerous events of cDC1 division (Figure 4D; Video S1). Next, in order to visualize the extension of the network from medulla toward the paracortex, we analyzed thick (200 μm) vibratome sections of LNs from these mice. We thereby discovered several examples of the developing cDC1 network extending around blood vessels from medulla into the paracortex (Figure 4E; Videos S2, S3, and S4). Next, we wished to address the consequences on cDC1 development if this population was experimentally retained in the medulla. Because CCR7 likely has a similar critical function for resident and migratory DCs to migrate to the paracortex during homeostatic maturation, we generated mixed BM chimeric mice (WT + *Ccr7* KO → WT) (Figure 4F). As expected, migratory cDC1s (CD8α^{-}CD103^{+}) in LNs were virtually absent among *Ccr7*-deficient cDC1s due to their inability to migrate from tissues (Figure S4A). Using the i.v. αXCR1 antibody labeling approach, we observed that *Ccr7*-deficient mature resident cDC1s were labeled at a significantly higher frequency compared with their WT counterparts (Figure 4F). This suggested that *Ccr7*-deficient resident cDC1s primarily remained within the LN medulla and in proximity to blood vessels even after their homeostatic maturation. Interestingly, the fraction of mature cells among resident *Ccr7*-deficient cDC1s was significantly lower compared with resident WT cDC1s (Figure 4G). This suggested that the impaired migration out of the medulla inhibited the homeostatic maturation of resident cDC1s and/or shortened the survival of mature resident cDC1s. Together, these data support a model in which the LN medulla provides a niche for cDC1 development. Additionally, it serves as a topographical starting point from which the cDC1 network unfolds, typically along blood vessels, toward the paracortex, as if on a conveyor belt.

Inflammation-induced DC maturation and relocalization disrupts their network

So far, we have elucidated how the resident cDC1 network evolves and spatially unfolds during homeostasis. Next, we wished to address how this network changes during inflammation. Following local skin infection with modified vaccinia virus Ankara (MVA), a large fraction of resident cDC1s matured and upregulated CD86 and CCR7 (Figures 5A and S5A), whereas the absolute numbers of cDC1s remained unchanged (Figure S5B). Accordingly, 24 h after viral infection or IFNα--driven maturation, we detected a significant translocation of cDC1s to the deep paracortex (Figures 5B and S5C). However, this synchronized response also revealed that key strategic positions (medulla/lymphatic sinuses) became temporarily devoid of cDC1s. Indeed, the uptake of fluorescently labeled protein (BSA-AF647) was significantly reduced 24 h after IFNα injection among resident cDC1s (Figures 5C–5E). This was not only due to cDC1 translocation and maturation, which is connected to a gradual decrease in their phagocytic capacity,[22] but was also seen among newly developing immature cDC1s in the medulla (Figures 5F and 5G). Together, these data showed that the majority of the LN-resident cDC1 population is maintained at a state of optimal responsiveness, allowing for a rapid and collective activation. On the other hand, the population-wide responsiveness temporarily impairs the LN to respond to consecutive challenges because it leaves only early developing, not fully functional cDC1s at strategic locations (Figure S5D). The question that subsequently arose was which local mechanisms may help to rapidly reestablish the network following infection?

cDC1 paucity in the medullary niche increases local Flt3L availability

We hypothesized that preDCs and immature cDC1s might sense their local abundance within the medullary niche and focused on Flt3L—a key cytokine for DC development. Systemic application of Flt3L for several days promotes preDC proliferation in the BM.[23] Similarly, a general paucity of cDCs leads to elevated systemic Flt3L levels, which, in a progenitor-progeny feedback mechanism, increases the preDC output from the BM.[24] However, this feedback mechanism only adapts the quantity of cDCs and not the developmental stage of an individual cell in the tissue. Therefore, we speculated that this cytokine might have an additional immediate function within the medullary niche. First, we asked whether local amounts of Flt3L are altered following infection. Upon Flt3L binding, its receptor CD135 is rapidly internalized and degraded.[25,26] Therefore, we measured CD135 surface expression on preDCs in LNs following viral infection as a proxy of Flt3L availability. Indeed, we observed a significant reduction of CD135 on preDCs that coincided with cDC maturation and exit from the medulla (Figure 6A). To refine our results, we analyzed *Zbtb46*^{GFP} mice to facilitate preDC identification. In line with our previous results, we observed a significant reduction of CD135 surface levels on preDCs in the dLN upon local IFNα application in the foot hock (Figure 6B), yet not in the BM or in non-dLNs (Figure S6A). Notably, Flt3L production in the dLN remained unaltered following IFNα application, based on mRNA levels from whole LN homogenates (Figure S6B). In the dLN we also observed a decrease of CD135 surface levels on immature cDC1s and cDC2s that still resided within the medullary niche, yet not on migratory cDC1s that populated the paracortex (Figures 6C, S6C, and S6D). Importantly, systemic Flt3L injection decreased CD135 levels on preDCs and immature and migratory cDC1s (Figures 6D and 6E). Therefore, these results indicated that the heightened Flt3L levels following infection or IFNα-induced maturation are locally sensed by preDCs and immature cDC1s and cDC2s in the medullary niche but not by migratory cDCs that populate the

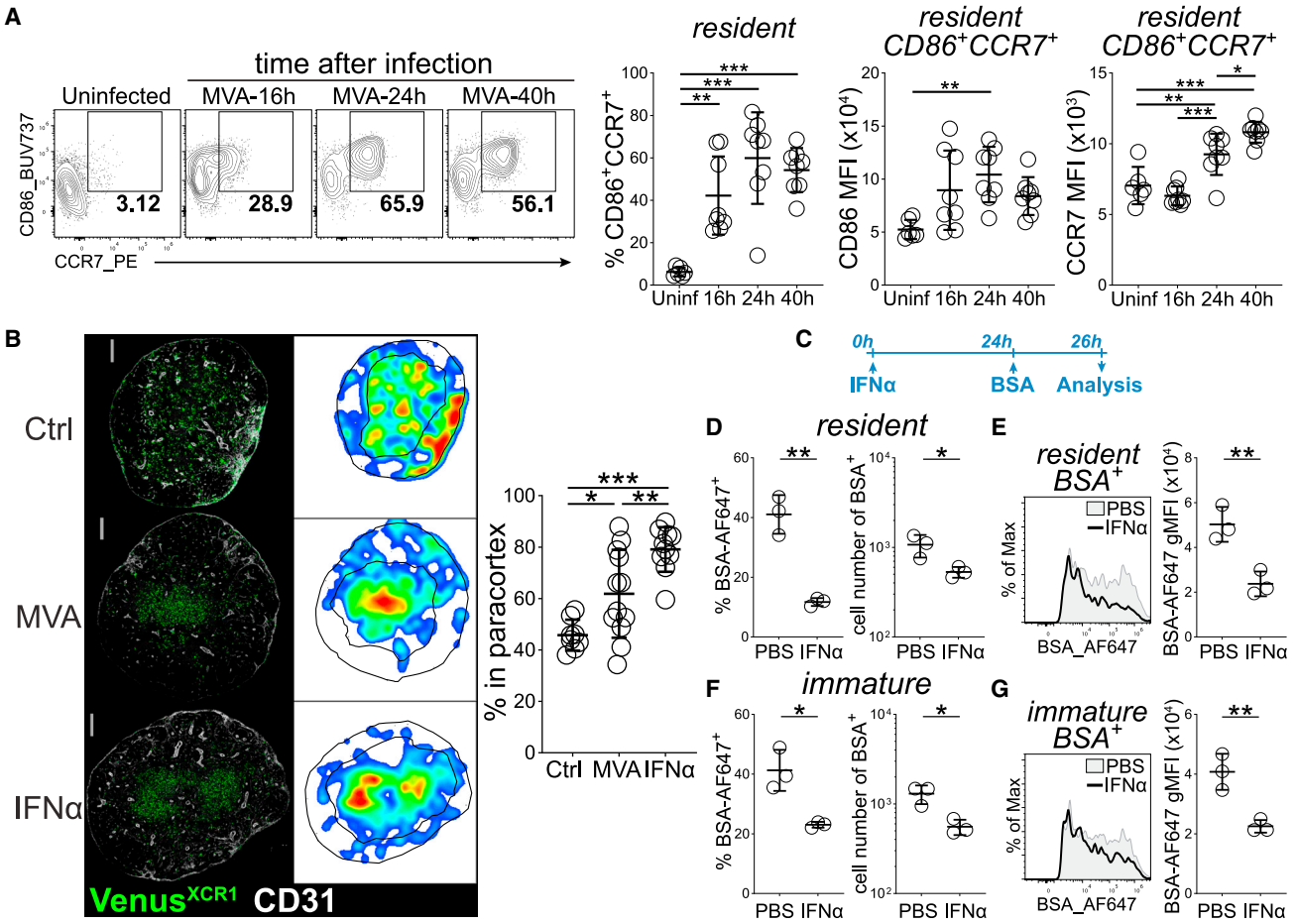

Figure 5. Synchronized migration of resident cDC1s during inflammation impairs LN functionality

(A) Flow cytometric analysis draining popliteal LNs of WT mice 16, 24, and 40 h after s.c. infection with MVA into the foot hock. Frequency of CD86$^+$CCR7$^+$ cells among resident (XCR1$^+$CD8α^+) cDC1s (left) and mean fluorescence intensity (MFI) values of CD86 and CCR7 among CD86$^+$CCR7$^+$ resident cDC1s (right).

(B) Localization of XCR1$^+$ cDC1s in popliteal LNs of *Xcr1*^{Venus} mice 24 h after s.c. infection with MVA or IFNα injection into the foot hock. Confocal microscopy (left), density plots showing the distribution of XCR1$^+$ cDC1s (middle, outer black line outlines the LN border and inner black line outlines the paracortex), and frequency of XCR1$^+$ cDC1s in the medulla (right).

(C–G) WT mice were injected with IFNα or PBS s.c. into the foot hock and 24 h later AF647-labeled BSA was injected s.c. into the foot hock and draining LNs were analyzed 2 h after BSA injection. Experimental setup (C), frequency of BSA$^+$ cells among resident (XCR1$^+$CD8α^+) cDC1s (left), and number of BSA$^+$ resident cDC1s (right) (D), BSA intensity among BSA$^+$ resident cDC1s (E), frequency of BSA$^+$ cells among immature (MHCII^{lo}CD24$^+$) cDC1s (left) and number of BSA$^+$ immature cDC1s (right) (F), and BSA intensity among BSA$^+$ immature cDC1s (G).

Images are representative of ≥2 independent experiments (B) and data display pooled data from ≥2 independent experiments (A–G) (A, n = 6–8; B, n = 4–6 using 2 LNs/n; C–G, n = 3). Error bars indicate the mean ± SD. Comparison between groups was calculated using one-way ANOVA or unpaired Student's t tests. ***p value < 0.001, **p value < 0.01, *p value < 0.05. Scale bars represent 200 μm in (B).

paracortex. Importantly, IFNα-induced loss of CD135 surface levels depended on Flt3L signaling and was blocked using Flt3 inhibitors *in vivo* (Figures 6F and S6E). Together, these results indicated that changes in cDC1 abundance and Flt3L consumers in the LN medulla are locally sensed via an altered availability of constitutively expressed Flt3L.

To test whether a change in cDC1 abundance is sufficient to mediate CD135 internalization, we depleted cDC1s in *Xcr1*^{DTR} mice and measured CD135 levels on preDCs in the LN over time (Figure 6G). 2 days after depletion, the CD135 surface levels on preDCs were dramatically reduced. Fittingly, with locally increasing numbers of cDC1s, the CD135 levels also continuously recovered on preDCs and immature cDC2s (Figures 6G and S6F). Importantly, we did not detect a difference in local production of Flt3L after depletion of cDC1s (Figure S6G). Finally, we generated mixed BM chimeric mice that allowed us to deplete 50% of cDC1s (*Xcr1*^{DTR} + *Xcr1*^{Venus} → WT) (Figure 6H). In line with our previous results, we observed a significant reduction in CD135 expression levels that matched a 50% reduction in cDC1 abundance (Figure 6G). This reduction was again seen on preDCs and immature resident cDC1s and cDC2s that resided in the medulla yet not on migratory cDC1s that populate the paracortex (Figures 6G, 6I, and S6H). Together, these results established that preDCs and immature cDCs within the medullary niche respond to changes in local cDC abundance via altered Flt3L signaling (Figure S6I).

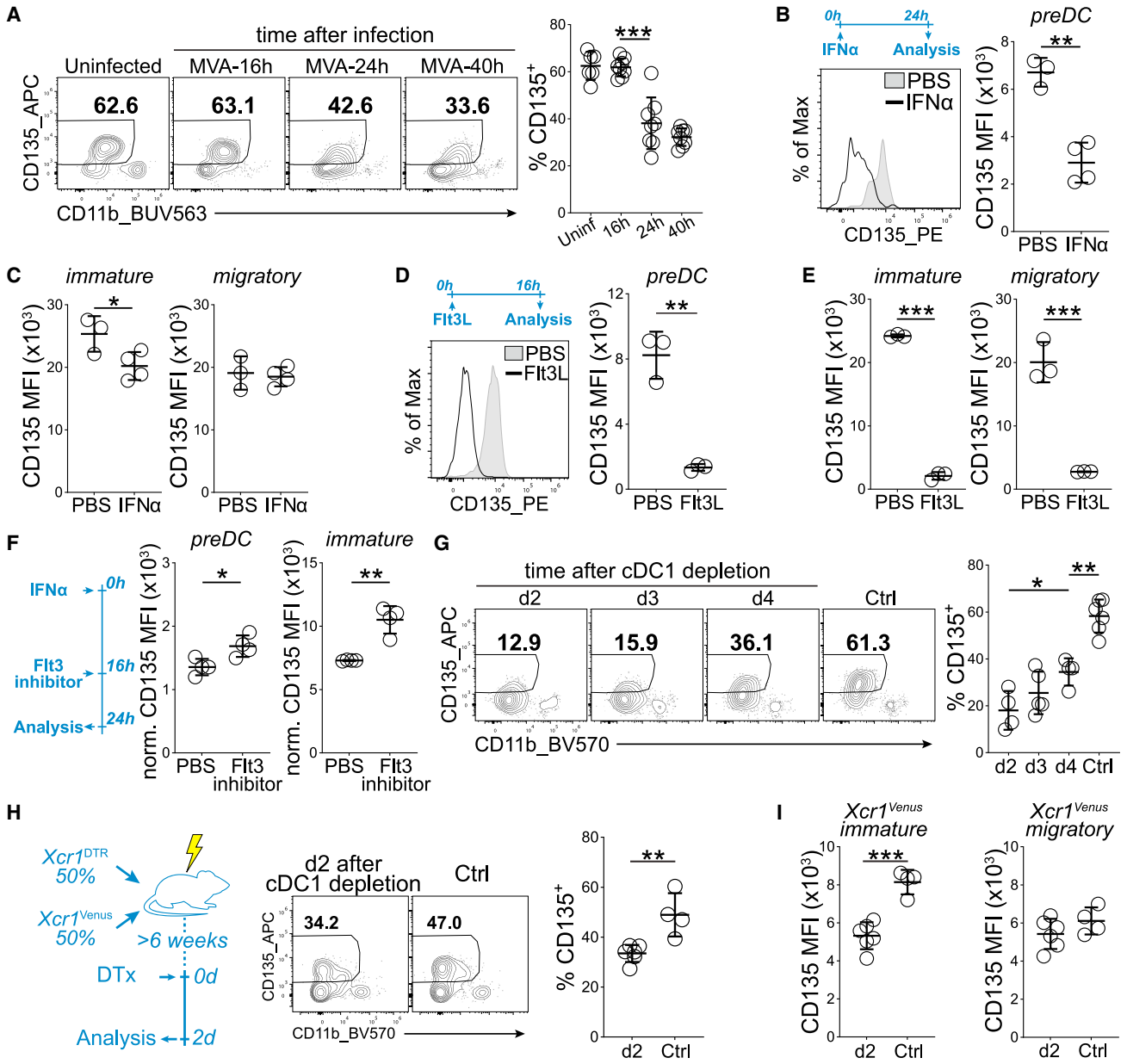

Figure 6. cDC1 abundance in the medulla is locally sensed by preDCs and immature cDCs via Flt3L availability

(A) Frequency of CD135$^+$ cells among CD11c$^+$MHCII$^-$ cells that contain preDCs in popliteal LNs of WT mice 16, 24, and 40 h after s.c. MVA infection into the foot hock.

(B and C) Surface CD135 expression among preDCs (CD11c$^+$MHCII$^-$) (B) and immature (MHCII^{lo}CD24$^+$, left) or migratory (XCR1$^+$CD8α^-CD103$^+$, right) cDC1s (C) in draining LNs of *Zbtb46*^{GFP} mice 24 h after s.c. IFNα injection into the foot hock.

(D and E) Surface CD135 expression among preDCs (CD11c$^+$MHCII$^-$) (D) and immature (MHCII^{lo}CD24$^+$, left) or migratory (XCR1$^+$CD8α^-CD103$^+$, right) cDC1s (E) in draining LNs of *Zbtb46*^{GFP} mice 16 h after i.p. Flt3L injection.

(F) Surface CD135 expression among preDCs (CD11c$^+$MHCII$^-$) (left) and immature (MHCII^{lo}CD24$^+$, right) cDC1s in draining LNs of WT mice 24 h after s.c. IFNα injection into the foot hock and 8 h after Flt3 inhibitor administration.

(G) Frequency of CD135$^+$ cells among CD11c$^+$MHCII$^-$ cells that contain preDCs in LNs of *Xcr1*^{DTR} mice 2, 3, and 4 days after cDC1 depletion with DTx injection.

(H and I) Mixed *Xcr1*^{DTR}:*Xcr1*^{Venus} (50:50) BM chimeras were treated with DTx 2 days before analysis to deplete only half of the cDC1 population. Frequency of CD135$^+$ cells among CD11c$^+$MHCII$^-$ cells that contain preDCs (H) and surface CD135 expression among *Xcr1*^{Venus} immature (MHCII^{lo}CD24$^+$XCR1$^+$, left) or migratory (XCR1$^+$CD8α^-CD103$^+$, right) cDC1s in LNs (I).

Data display pooled data from ≥2 independent experiments (A–I) (A, n = 6–8; B and C, n = 3–4; D and E, n = 3; F, n = 4; G, n = 4–6; H and I, n = 4–6). Error bars indicate the mean ± SD. Comparison between groups was calculated using one-way ANOVA or unpaired Student's t tests. ***p value < 0.001, **p value < 0.01, *p value < 0.05.

A local Flt3L feedback in the medulla regulates the developmental speed of cDC1s

Next, we hypothesized that enhanced Flt3L signaling accelerates cDC1 development in the LN to rapidly reestablish the cDC1 network and thereby LN functionality. Therefore, we crossed *Prtn3*$^{LSL\text{-}Tom}$ mice with *Xcr1*^{DTR}, allowing us to track and compare the development of cDC1s in the steady state and following their depletion. When comparing Tomato-labeled developing cDC1s, we observed a significant relative reduction in developmentally early stages in depleted (day 3) vs. non-depleted mice (Figures 7A and 7B). Additionally, when analyzing a later time point (day 5) post-depletion, we observed a significant increase in MHCII and CD11c levels on immature cDC1s (Figure 7C). Next, we isolated preDCs from the BM of *Zbtb46*^{GFP} mice, transferred them into cDC1-depleted or WT animals, and analyzed their phenotype 3 days later (Figures 7D, S7A, and S7B). Supporting our prior results, we detected higher levels of MHCII, CD11c, and XCR1 if preDCs were transferred into cDC1-depleted mice (Figure 7D). Next, to investigate causality, we injected Flt3L into *Zbtb46*^{GFP} mice (Figures 7E, 7F, and S7C). 16 h after systemic Flt3L injection, we did not observe an increase in absolute numbers in cDC1s and cDC2s (Figure S7D). Yet, we detected an accelerated development of preDCs along the cDC1 trajectory, as indicated by relative loss of preDCs (Figure 7E), and an increase in MHCII, CD11c, and XCR1 expression levels among immature cDC1s (Figure 7F). Short-term local injection of Flt3L in the foot hock decreased CD135 levels and increased CD11c expression on immature cDC1s in the dLN yet not in contralateral LNs (Figures 7G and 7H). Finally, we treated *Prtn3*$^{LSL\text{-}Tom}$ mice with tamoxifen and injected Flt3L. When analyzing Tomato^{+} cDCs in LNs 16 h later, we again observed an accelerated cDC1 development with a relative loss of preDCs and an increase in MHCII, CD11c, and XCR1 expression levels (Figures 7I–7K). Collectively, these results showed that the LN medulla functions as a niche that allows for local Flt3L feedback to cDC abundance. Elevated medullary Flt3L levels following cDC1 exit from this niche in turn accelerated the development of newly arriving preDCs and immature cDC1s to rapidly reestablish a fully responsive network (Figure S7E).

DISCUSSION

By studying the principles of cDC1 network development, we found the following sequence of events. PreDCs predominantly enter the LN via medullary HEVs and gradually develop into immature cDC1s, a process that takes approximately 4 days and involves the increased expression of proteins critical for optimal function. The medulla acts as a cradle for local cDC1 development and as the topographic starting point of the cDC1 network. The blood vessels that traverse the LN parenchyma and converge in the medulla serve as a scaffold along which the network unfolds with concomitant differentiation of cDC1s. Thereby, resident cDC1s form a network that is spatially and functionally distinct from the migrating cDC1s that arrive via the afferent lymphatics and then migrate through interfollicular regions into the paracortex. Upon inflammation in the LN, the medulla-resident cDC1s mature and migrate via CCR7 to the paracortex, where they now coalesce with the migrating cDC1s. This, in turn, leaves gaps in the remaining cDC1 network that are sensed by newly arriving preDCs in the medulla via locally increased availability of Flt3L. The increased local exposure to Flt3L, in turn, accelerates cDC1 development to rapidly restore the network. These results reveal a compensatory mechanism for maintaining functional cDC1 populations based on a feedback loop between local cDC1 abundance and Flt3L availability.

Several principles that we uncovered for immature cDC1s may also apply to immature cDC2 development, which also reside in the LN medulla.[27] How cDC2 networks evolve from a spatial and temporal perspective is, however, unclear. cDC2s appear to be independent from extrinsic Flt3L signals and cell-autonomously produce and sense this critical cytokine.[28] Therefore, we presume that cDC1 and cDC2 networks are largely maintained independently. Nevertheless, it seems probable that cDC2 maintenance and abundance in LNs follows a similar concept as shown here for cDC1s, but if similar local feedback is active, it is likely mediated via a different set of cytokines, such as colony stimulating factor 1 (CSF1), stem cell factor (SCF), or lymphotoxins.[29,30]

Arterioles enter the LN via the medulla, give rise to a network of capillaries, and form a loop while they transform into paracortical HEV (order III–V).[31] These HEVs merge and form higher order vessels (order I–II) in the medulla and exit the LN as medullary veins.[32] Our finding that preDCs preferentially enter LNs via lower order medullary rather than higher paracortical HEVs is in line with a previous study.[15] However, we could not confirm a strict dependence on CD62L in this process, which requires further testing on a genetic level in the future.[32] Once extravasated, developing preDCs and cDC1s use blood vessels or the surrounding connective tissue as structural guidance on their way to the paracortex.[33] The chemotactic factor(s) that promotes this migration is currently unclear.

The LN medulla functions as a cradle for cDC1 and cDC2 development, and recent results indicate that medullary cords, along with the cortex-medullary boundary, are populated by distinct groups of fibroblastic reticular cells.[34] The spleen lacks a structure that recapitulates the LN medulla; yet, the splenic red pulp might also include local vascular niches and stromal cells that guide the development of immigrating preDCs, as shown here in the LN.[35–37] Similarly, blood vessels and their surrounding connective tissues are likely structural and functional niches that promote the spatiotemporal development of three-dimensional cDC networks in non-lymphoid organs.[6] Further characterization of these niches will be critical to therapeutically modify cDC networks in tissues. For example, cDC1 abundance in tumors is a positive prognostic marker, which is reflected by their key role in orchestrating anti-tumor immunity of cytotoxic lymphocytes, such as CD8^{+} T cells and NK cells.[38,39]

PreDCs show lineage commitment in the BM.[7,40] Analysis of DC clonality in tissues further identified mixed fates among clones suggesting the presence of uncommitted preDCs in tissues.[6] In LNs, we readily identified committed preDC1s and preDC2s and yet did not detect an uncommitted preDC population using scRNA-seq. Notably, this analysis further showed that bona fide preDCs comprise only a very small population within a CD11c^{+}MHCII^{-}CD135^{+} gate, which is typically used to identify preDCs via flow cytometry. We further found that preDC1s

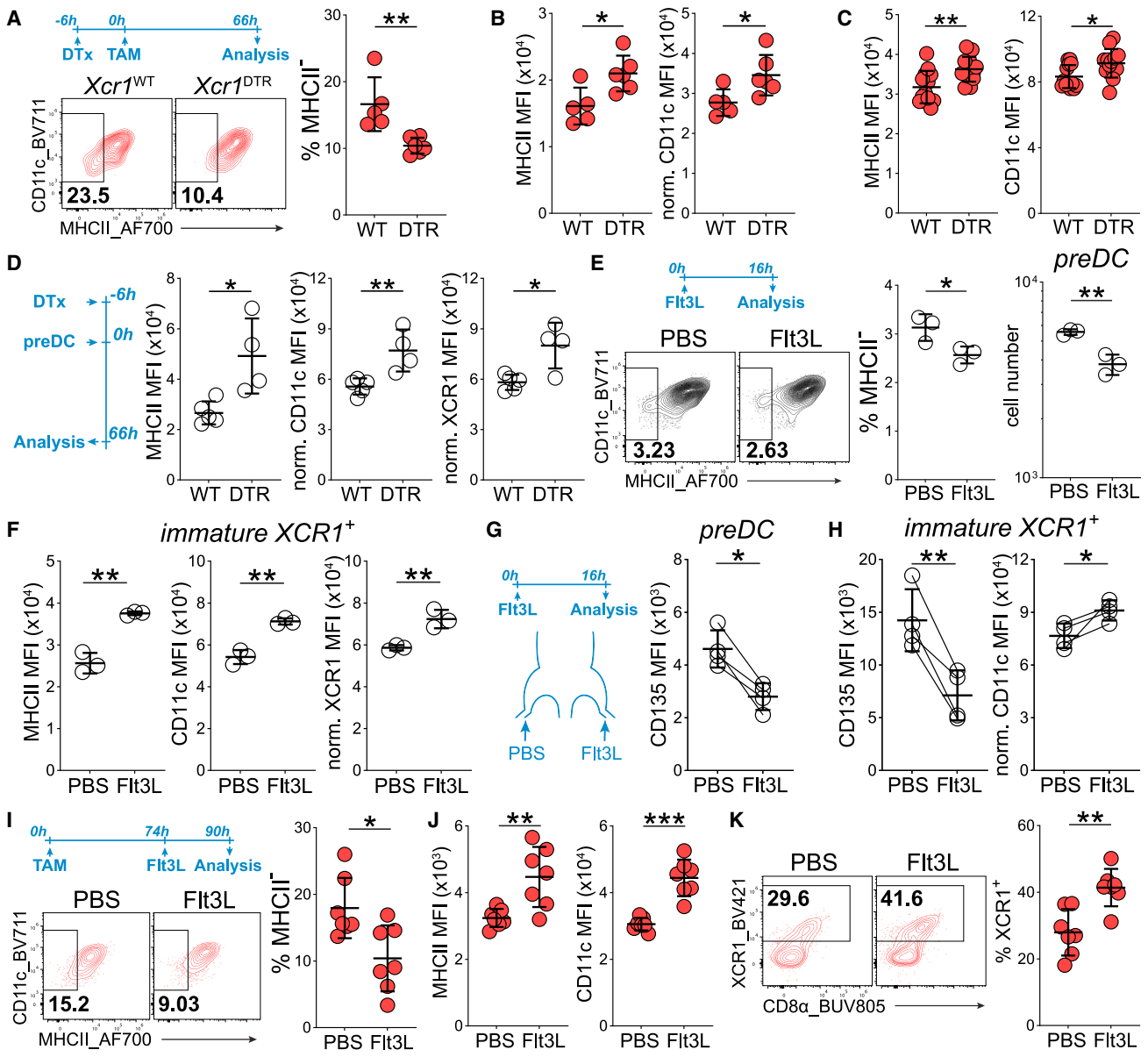

Figure 7. Increased Flt3L signaling accelerates local cDC1 development

(A and B) *Prtn3*$^{LSL\text{-}Tom}$*Xcr1*^{WT} or *Prtn3*$^{LSL\text{-}Tom}$*Xcr1*^{DTR} mice received DTx and tamoxifen according to the indicated scheme to analyze cDC1 development in LNs after cDC1 depletion. Frequency of MHCII^{-} cells (A) and expression of MHCII and CD11c among Tomato^{+} immature/developing (MHCII$^{-/lo}$CD24^{+}) cDC1s in LNs (B).

(C) *Prtn3*$^{LSL\text{-}Tom}$*Xcr1*^{WT} or *Prtn3*$^{LSL\text{-}Tom}$*Xcr1*^{DTR} mice received DTx at −6 h, tamoxifen at 0 h, and analyzed 5 days after depletion, similar to the experimental setup in (A). Expression of MHCII and CD11c among Tomato^{+} immature (MHCII^{lo}CD24^{+}) cDC1s in LNs.

(D) PreDCs from the BM of *Zbtb46*^{GFP} mice were transferred into *Xcr1*^{WT} or *Xcr1*^{DTR} mice after depletion and analyzed 66 h after transfer. Expression of MHCII, CD11c and XCR1 among transferred GFP^{+} immature (MHCII^{lo}CD24^{+}XCR1^{+}) cDC1s in LNs (right).

(E and F) Analysis of LNs of *Zbtb46*^{GFP} mice 16 h after i.p. Flt3L injection. Frequency of preDCs among immature/developing (MHCII$^{-/lo}$) cDCs (left), cell numbers of preDCs (right) (E), and expression of MHCII, CD11c, and XCR1 among immature (MHCII^{lo}CD24^{+}XCR1^{+}) cDC1s in LNs (F).

(G and H) Analysis of draining LNs of *Zbtb46*^{GFP} mice 16 h after s.c. Flt3L injection into the foot hock. Surface CD135 expression among preDCs (G) and surface CD135 and CD11c expression among immature (MHCII^{lo}CD24^{+}XCR1^{+}) cDC1s in draining LNs (H).

(I–K) *Prtn3*$^{LSL\text{-}Tom}$ mice received tamoxifen and Flt3L according to the indicated scheme. Frequency of MHCII^{-} cells (I) and expression of MHCII and CD11c (J) and frequency of XCR1^{+} cells among Tomato^{+} immature/developing (MHCII$^{-/lo}$CD24^{+}) cDC1s in LNs (K).

Data display pooled data from ≥2 independent experiments (A–K) (A and B, n = 5–6; C, n = 13; D, n = 4–5; E and F, n = 3; G and H, n = 4; I–K, n = 7). Error bars indicate the mean ± SD. Comparison between groups was calculated using paired or unpaired Student's t tests. ***p value < 0.001, **p value < 0.01, *p value < 0.05.

followed a straight developmental path toward cDC1s. This is in stark contrast to the development of preDC2s, which are highly plastic and can lead to different fates ranging from cDC2 subsets to pDCs and transitional populations.[20,41–43] Recent evidence indicates that a substantial fraction of cDC2s arise from pDC-like cells, whereas our results suggest an opposite developmental trajectory is also possible.[44] Nevertheless, we have also seen heterogeneity among preDC2s in LNs using our *Prtn3* fate-mapping system combined with scRNA-seq analysis. Therefore, it seems possible that some of these fates, or at least a significant bias, are already predetermined at the preDC2 level, as previously suggested.[45–47]

The development of macrophage networks and their maintenance underlies a different mechanism, as shown here for cDC1s. Upon experimental or inflammation-induced loss of macrophages in tissues, monocytes are rapidly recruited in large numbers and compete for distinct topographically restricted niches.[12,48] By contrast, the niche that supports the dynamic cDC network that we investigated here rather resembles a conveyor belt—a dynamic niche that provides structure but also regulates developmental progression of its associated cells. This dynamic niche can act not only as a compensatory mechanism to fill gaps in the DC network during infections but also to maintain a constant number of fully developed DCs at steady state.

In summary, the findings herein uncover basic principles of the development and regulation of a dynamic cDC network within a shared niche, in contrast to macrophage networks that are composed of cells that populate individual niches. We believe that these principles may guide future approaches to therapeutically manipulate cDC networks to maximize or dampen adaptive immune responses.

Limitations of the study

Our conveyor belt model is based on indirect evidence using genetic fate-tracking models that indicate immature cDC1 movement toward the paracortex as they develop. This migration takes place over a period of days; therefore, unfortunately, we were not able to directly visualize this process by intravital microscopy. Our results suggest that medullary HEVs recruit both preDC1s and preDC2s and the medulla functions as a general niche for all developing cDC1s and cDC2s. However, in the absence of definitive genetic tools for cDC2 identification, this conclusion remains, in part, speculative. Notably, we could not detect increased intracellular CD135 levels following Flt3L binding and subsequent CD135 internalization, likely due to rapid degradation. Although our data strongly suggest internalization of CD135 due to increased availability of Flt3L, inflammatory mediators might directly or indirectly modulate CD135 levels. Finally, the applied Flt3L inhibitors are not fully selective and may also inhibit other receptor tyrosine kinases.

STAR★METHODS

Detailed methods are provided in the online version of this paper and include the following:

SUPPLEMENTAL INFORMATION

Supplemental information can be found online at https://doi.org/10.1016/j.immuni.2023.06.020.

ACKNOWLEDGMENTS

This work was supported by the Bavarian Ministry of Economic Affairs, Regional Development and Energy within the project "Single cell analysis in personalized medicine" at the Helmholtz-Institute for RNA-Based Infection Research implemented in the Single-Cell Center Würzburg. We would like to thank the Core Unit for FACS and the Core Unit SysMed of the IZKF Würzburg, R. Förster, and I. Ravens from MHH for *Ccr7*$^{-/-}$ BM and D. Akkar and P. Penndorf for technical assistance. This work was supported by a fellowship through the German Research Foundation (DFG) (UG 61/2-1 to M.U.) and grants of the European Research Council (ERC) to W.K. (819329-STEP2) and G. Gasteiger (759176-TissueLymphoContexts). W.K. and G. Gasteiger are supported by the Max Planck Society (Max Planck Research Groups).

AUTHOR CONTRIBUTIONS

M.U. and W.K. conceptualized the study. M.U., R.J.L., C.F., K.K., K.J., G. Golda, K.H., and A.G. planned and performed experiments and/or analyzed the data. K.K., F.I., G. Golda, A.-E.S., and D.G. generated and/or analyzed transcriptome data. T.K. provided critical reagents. M.B. and G. Gasteiger provided intellectual input and gave conceptual advice. W.K. and M.U. wrote the manuscript with input from all authors. G. Gasteiger and W.K. provided research funds.

DECLARATION OF INTERESTS

The authors declare no competing interests.

Received: October 31, 2022
Revised: April 2, 2023
Accepted: June 21, 2023
Published: July 17, 2023

REFERENCES

1. Cabeza-Cabrerizo, M., Cardoso, A., Minutti, C.M., Pereira da Costa, M., and Reis e Sousa, C. (2021). Dendritic cells revisited. Annu. Rev. Immunol. *39*, 131–166. https://doi.org/10.1146/annurev-immunol-061020-053707.
2. Steinman, R.M. (2012). Decisions about dendritic cells: past, present, and future. Annu. Rev. Immunol. *30*, 1–22. https://doi.org/10.1146/annurev-immunol-100311-102839.
3. Wculek, S.K., Cueto, F.J., Mujal, A.M., Melero, I., Krummel, M.F., and Sancho, D. (2020). Dendritic cells in cancer immunology and immunotherapy. Nat. Rev. Immunol. *20*, 7–24. https://doi.org/10.1038/s41577-019-0210-z.
4. Dudziak, D., Kamphorst, A.O., Heidkamp, G.F., Buchholz, V.R., Trumpfheller, C., Yamazaki, S., Cheong, C., Liu, K., Lee, H.W., Park, C.G., et al. (2007). Differential antigen processing by dendritic cell subsets in vivo. Science *315*, 107–111. https://doi.org/10.1126/science.1136080.
5. Vander Lugt, B., Khan, A.A., Hackney, J.A., Agrawal, S., Lesch, J., Zhou, M., Lee, W.P., Park, S., Xu, M., DeVoss, J., et al. (2014). Transcriptional programming of dendritic cells for enhanced MHC class II antigen presentation. Nat. Immunol. *15*, 161–167. https://doi.org/10.1038/ni.2795.
6. Cabeza-Cabrerizo, M., van Blijswijk, J., Wienert, S., Heim, D., Jenkins, R.P., Chakravarty, P., Rogers, N., Frederico, B., Acton, S., Beerling, E., et al. (2019). Tissue clonality of dendritic cell subsets and emergency DCpoiesis revealed by multicolor fate mapping of DC progenitors. Sci. Immunol. *4*, eaaw1941. https://doi.org/10.1126/sciimmunol.aaw1941.
7. Schlitzer, A., Sivakamasundari, V., Chen, J., Sumatoh, H.R., Schreuder, J., Lum, J., Malleret, B., Zhang, S., Larbi, A., Zolezzi, F., et al. (2015). Identification of cDC1- and cDC2-committed DC progenitors reveals early lineage priming at the common DC progenitor stage in the bone marrow. Nat. Immunol. *16*, 718–728. https://doi.org/10.1038/ni.3200.
8. Alexandre, Y.O., Ghilas, S., Sanchez, C., Le Bon, A., Crozat, K., and Dalod, M. (2016). XCR1+ dendritic cells promote memory CD8+ T cell recall upon secondary infections with Listeria monocytogenes or certain viruses. J. Exp. Med. *213*, 75–92. https://doi.org/10.1084/jem.20142350.
9. Brewitz, A., Eickhoff, S., Dähling, S., Quast, T., Bedoui, S., Kroczek, R.A., Kurts, C., Garbi, N., Barchet, W., Iannacone, M., et al. (2017). CD8(+) T cells orchestrate pDC-XCR1(+) dendritic cell spatial and functional cooperativity to optimize priming. Immunity *46*, 205–219. https://doi.org/10.1016/j.immuni.2017.01.003.
10. Ghilas, S., Ambrosini, M., Cancel, J.C., Brousse, C., Massé, M., Lelouard, H., Dalod, M., and Crozat, K. (2021). Natural killer cells and dendritic epidermal gammadelta T cells orchestrate type 1 conventional DC spatiotemporal repositioning toward CD8(+) T cells. iScience. iScience *24*, 103059. https://doi.org/10.1016/j.isci.2021.103059.
11. Kamath, A.T., Henri, S., Battye, F., Tough, D.F., and Shortman, K. (2002). Developmental kinetics and lifespan of dendritic cells in mouse lymphoid organs. Blood *100*, 1734–1741.
12. Guilliams, M., Thierry, G.R., Bonnardel, J., and Bajenoff, M. (2020). Establishment and maintenance of the macrophage niche. Immunity *52*, 434–451. https://doi.org/10.1016/j.immuni.2020.02.015.
13. Woodruff, M.C., Heesters, B.A., Herndon, C.N., Groom, J.R., Thomas, P.G., Luster, A.D., Turley, S.J., and Carroll, M.C. (2014). Trans-nodal migration of resident dendritic cells into medullary interfollicular regions initiates immunity to influenza vaccine. J. Exp. Med. *211*, 1611–1621. https://doi.org/10.1084/jem.20132327.
14. Lindquist, R.L., Shakhar, G., Dudziak, D., Wardemann, H., Eisenreich, T., Dustin, M.L., and Nussenzweig, M.C. (2004). Visualizing dendritic cell networks in vivo. Nat. Immunol. *5*, 1243–1250. https://doi.org/10.1038/ni1139.
15. Liu, K., Waskow, C., Liu, X., Yao, K., Hoh, J., and Nussenzweig, M. (2007). Origin of dendritic cells in peripheral lymphoid organs of mice. Nat. Immunol. *8*, 578–583. https://doi.org/10.1038/ni1462.
16. Guilliams, M., Dutertre, C.A., Scott, C.L., McGovern, N., Sichien, D., Chakarov, S., Van Gassen, S., Chen, J., Poidinger, M., De Prijck, S., et al. (2016). Unsupervised high-dimensional analysis aligns dendritic cells across tissues and species. Immunity *45*, 669–684. https://doi.org/10.1016/j.immuni.2016.08.015.
17. Mattiuz, R., Wohn, C., Ghilas, S., Ambrosini, M., Alexandre, Y.O., Sanchez, C., Fries, A., Vu Manh, T.P., Malissen, B., Dalod, M., and Crozat, K. (2018). Novel Cre-expressing mouse strains permitting to selectively track and edit Type 1 conventional dendritic cells facilitate disentangling their complexity in vivo. Front. Immunol. *9*, 2805. https://doi.org/10.3389/fimmu.2018.02805.
18. Durai, V., Bagadia, P., Granja, J.M., Satpathy, A.T., Kulkarni, D.H., Davidson, J.T.t., Wu, R., Patel, S.J., Iwata, A., Liu, T.T., et al. (2019). Cryptic activation of an Irf8 enhancer governs cDC1 fate specification. Nat. Immunol. *20*, 1161–1173. https://doi.org/10.1038/s41590-019-0450-x.
19. Schlitzer, A., Heiseke, A.F., Einwächter, H., Reindl, W., Schiemann, M., Manta, C.P., See, P., Niess, J.H., Suter, T., Ginhoux, F., and Krug, A.B. (2012). Tissue-specific differentiation of a circulating CCR9- pDC-like common dendritic cell precursor. Blood *119*, 6063–6071. https://doi.org/10.1182/blood-2012-03-418400.
20. Leylek, R., Alcántara-Hernández, M., Lanzar, Z., Lüdtke, A., Perez, O.A., Reizis, B., and Idoyaga, J. (2019). Integrated cross-species analysis identifies a conserved transitional dendritic cell population. Cell Rep. *29*, 3736–3750.e8. https://doi.org/10.1016/j.celrep.2019.11.042.
21. Liu, K., Victora, G.D., Schwickert, T.A., Guermonprez, P., Meredith, M.M., Yao, K., Chu, F.F., Randolph, G.J., Rudensky, A.Y., and Nussenzweig, M. (2009). In vivo analysis of dendritic cell development and homeostasis. Science *324*, 392–397. https://doi.org/10.1126/science.1170540.
22. Alloatti, A., Kotsias, F., Magalhaes, J.G., and Amigorena, S. (2016). Dendritic cell maturation and cross-presentation: timing matters! Immunol. Rev. *272*, 97–108. https://doi.org/10.1111/imr.12432.
23. Pulendran, B., Lingappa, J., Kennedy, M.K., Smith, J., Teepe, M., Rudensky, A., Maliszewski, C.R., and Maraskovsky, E. (1997). Developmental pathways of dendritic cells in vivo: distinct function, phenotype, and localization of dendritic cell subsets in FLT3 ligand-treated mice. J. Immunol. *159*, 2222–2231.
24. Birnberg, T., Bar-On, L., Sapoznikov, A., Caton, M.L., Cervantes-Barragán, L., Makia, D., Krauthgamer, R., Brenner, O., Ludewig, B., Brockschnieder, D., et al. (2008). Lack of conventional dendritic cells is compatible with normal development and T cell homeostasis, but causes myeloid proliferative syndrome. Immunity *29*, 986–997. https://doi.org/10.1016/j.immuni.2008.10.012.
25. Cueto, F.J., and Sancho, D. (2021). The Flt3L/Flt3 axis in dendritic cell biology and cancer immunotherapy. Cancers (Basel) *13*, 1525. https://doi.org/10.3390/cancers13071525.
26. Turner, A.M., Lin, N.L., Issarachai, S., Lyman, S.D., and Broudy, V.C. (1996). FLT3 receptor expression on the surface of normal and malignant human hematopoietic cells. Blood *88*, 3383–3390.
27. Gerner, M.Y., Kastenmuller, W., Ifrim, I., Kabat, J., and Germain, R.N. (2012). Histo-cytometry: a method for highly multiplex quantitative tissue imaging analysis applied to dendritic cell subset microanatomy in lymph nodes. Immunity *37*, 364–376. https://doi.org/10.1016/j.immuni.2012.07.011.
28. Fujita, K., Chakarov, S., Kobayashi, T., Sakamoto, K., Voisin, B., Duan, K., Nakagawa, T., Horiuchi, K., Amagai, M., Ginhoux, F., and Nagao, K. (2019). Cell-autonomous FLT3L shedding via ADAM10 mediates conventional dendritic cell development in mouse spleen. Proc. Natl. Acad. Sci. USA *116*, 14714–14723. https://doi.org/10.1073/pnas.1818907116.
29. Durai, V., Bagadia, P., Briseño, C.G., Theisen, D.J., Iwata, A., Davidson, J.T.t., Gargaro, M., Fremont, D.H., Murphy, T.L., and Murphy, K.M. (2018). Altered compensatory cytokine signaling underlies the discrepancy between Flt3(-/-) and Flt3l(-/-) mice. J. Exp. Med. *215*, 1417–1435. https://doi.org/10.1084/jem.20171784.
30. Kabashima, K., Banks, T.A., Ansel, K.M., Lu, T.T., Ware, C.F., and Cyster, J.G. (2005). Intrinsic lymphotoxin-beta receptor requirement for

homeostasis of lymphoid tissue dendritic cells. Immunity *22*, 439–450. https://doi.org/10.1016/j.immuni.2005.02.007.

31. von Andrian, U.H. (1996). Intravital microscopy of the peripheral lymph node microcirculation in mice. Microcirculation *3*, 287–300. https://doi.org/10.3109/10739689609148303.
32. M'Rini, C., Cheng, G., Schweitzer, C., Cavanagh, L.L., Palframan, R.T., Mempel, T.R., Warnock, R.A., Lowe, J.B., Quackenbush, E.J., and von Andrian, U.H. (2003). A novel endothelial L-selectin ligand activity in lymph node medulla that is regulated by alpha(1,3)-fucosyltransferase-IV. J. Exp. Med. *198*, 1301–1312. https://doi.org/10.1084/jem.20030182.
33. Stoltzfus, C.R., Filipek, J., Gern, B.H., Olin, B.E., Leal, J.M., Wu, Y., Lyons-Cohen, M.R., Huang, J.Y., Paz-Stoltzfus, C.L., Plumlee, C.R., et al. (2020). CytoMAP: A spatial analysis toolbox reveals features of myeloid cell organization in lymphoid tissues. Cell Rep. *31*, 107523. https://doi.org/10.1016/j.celrep.2020.107523.
34. Takeuchi, A., Ozawa, M., Kanda, Y., Kozai, M., Ohigashi, I., Kurosawa, Y., Rahman, M.A., Kawamura, T., Shichida, Y., Umemoto, E., et al. (2018). A distinct subset of fibroblastic stromal cells constitutes the cortex-medulla boundary subcompartment of the lymph node. Front. Immunol. *9*, 2196. https://doi.org/10.3389/fimmu.2018.02196.
35. Alexandre, Y.O., Schienstock, D., Lee, H.J., Gandolfo, L.C., Williams, C.G., Devi, S., Pal, B., Groom, J.R., Cao, W., Christo, S.N., et al. (2022). A diverse fibroblastic stromal cell landscape in the spleen directs tissue homeostasis and immunity. Sci. Immunol. *7*, eabj0641. https://doi.org/10.1126/sciimmunol.abj0641.
36. Pezoldt, J., Wiechers, C., Erhard, F., Rand, U., Bulat, T., Beckstette, M., Brendolan, A., Huehn, J., Kalinke, U., Mueller, M., et al. (2021). Single-cell transcriptional profiling of splenic fibroblasts reveals subset-specific innate immune signatures in homeostasis and during viral infection. Commun. Biol. *4*, 1355. https://doi.org/10.1038/s42003-021-02882-9.
37. Bosteels, V., Maréchal, S., De Nolf, C., Rennen, S., Maelfait, J., Tavernier, S.J., Vetters, J., Van De Velde, E., Fayazpour, F., Deswarte, K., et al. (2023). LXR signaling controls homeostatic dendritic cell maturation. Sci. Immunol. *8*, eadd3955. https://doi.org/10.1126/sciimmunol.add3955.
38. Böttcher, J.P., Bonavita, E., Chakravarty, P., Blees, H., Cabeza-Cabrerizo, M., Sammicheli, S., Rogers, N.C., Sahai, E., Zelenay, S., and Reis e Sousa, C. (2018). NK cells stimulate recruitment of cDC1 into the tumor microenvironment promoting cancer immune control. Cell *172*, 1022–1037.e14. https://doi.org/10.1016/j.cell.2018.01.004.
39. Roberts, E.W., Broz, M.L., Binnewies, M., Headley, M.B., Nelson, A.E., Wolf, D.M., Kaisho, T., Bogunovic, D., Bhardwaj, N., and Krummel, M.F. (2016). Critical role for CD103(+)/CD141(+) dendritic cells bearing CCR7 for tumor antigen trafficking and priming of T cell immunity in melanoma. Cancer Cell *30*, 324–336. https://doi.org/10.1016/j.ccell.2016.06.003.
40. Grajales-Reyes, G.E., Iwata, A., Albring, J., Wu, X., Tussiwand, R., Kc, W., Kretzer, N.M., Briseño, C.G., Durai, V., Bagadia, P., et al. (2015). Batf3 maintains autoactivation of Irf8 for commitment of a CD8alpha(+) conventional DC clonogenic progenitor. Nat. Immunol. *16*, 708–717. https://doi.org/10.1038/ni.3197.
41. Brown, C.C., Gudjonson, H., Pritykin, Y., Deep, D., Lavallée, V.P., Mendoza, A., Fromme, R., Mazutis, L., Ariyan, C., Leslie, C., et al. (2019). Transcriptional basis of mouse and human dendritic cell heterogeneity. Cell *179*, 846–863.e24. https://doi.org/10.1016/j.cell.2019.09.035.
42. Lewis, K.L., Caton, M.L., Bogunovic, M., Greter, M., Grajkowska, L.T., Ng, D., Klinakis, A., Charo, I.F., Jung, S., Gommerman, J.L., et al. (2011). Notch2 receptor signaling controls functional differentiation of dendritic cells in the spleen and intestine. Immunity *35*, 780–791. https://doi.org/10.1016/j.immuni.2011.08.013.
43. Tussiwand, R., Everts, B., Grajales-Reyes, G.E., Kretzer, N.M., Iwata, A., Bagaitkar, J., Wu, X., Wong, R., Anderson, D.A., Murphy, T.L., et al. (2015). Klf4 expression in conventional dendritic cells is required for T helper 2 cell responses. Immunity *42*, 916–928. https://doi.org/10.1016/j.immuni.2015.04.017.
44. Rodrigues, P.F., Kouklas, A., Cvijetic, G., Bouladoux, N., Mitrovic, M., Desai, J.V., Lima-Junior, D.S., Lionakis, M.S., Belkaid, Y., Ivanek, R., et al. (2023). pDC-like cells are pre-DC2 and require KLF4 to control homeostatic CD4 T cells. Sci. Immunol. *8*, eadd4132. https://doi.org/10.1126/sciimmunol.add4132.
45. Guermonprez, P., Gerber-Ferder, Y., Vaivode, K., Bourdely, P., and Helft, J. (2019). Origin and development of classical dendritic cells. Int. Rev. Cell Mol. Biol. *349*, 1–54. https://doi.org/10.1016/bs.ircmb.2019.08.002.
46. Sichien, D., Lambrecht, B.N., Guilliams, M., and Scott, C.L. (2017). Development of conventional dendritic cells: from common bone marrow progenitors to multiple subsets in peripheral tissues. Mucosal Immunol. *10*, 831–844. https://doi.org/10.1038/mi.2017.8.
47. Chen, B., Zhu, L., Yang, S., and Su, W. (2021). Unraveling the heterogeneity and ontogeny of dendritic cells using single-cell RNA sequencing. Front. Immunol. *12*, 711329. https://doi.org/10.3389/fimmu.2021.711329.
48. Guilliams, M., and Scott, C.L. (2017). Does niche competition determine the origin of tissue-resident macrophages? Nat. Rev. Immunol. *17*, 451–460. https://doi.org/10.1038/nri.2017.42.
49. Himly, M., Foster, D.N., Bottoli, I., Iacovoni, J.S., and Vogt, P.K. (1998). The DF-1 chicken fibroblast cell line: transformation induced by diverse oncogenes and cell death resulting from infection by avian leukosis viruses. Virology *248*. https://doi.org/10.1006/viro.1998.9290.
50. Janowska-Wieczorek, A., Majka, M., Kijowski, J., Baj-Krzyworzeka, M., Reca, R., Turner, A.R., Ratajczak, J., Emerson, S.G., Kowalska, M.A., and Ratajczak, M.Z. (2001). Platelet-derived microparticles bind to hematopoietic stem/progenitor cells and enhance their engraftment. Blood, 98. https://doi.org/10.1182/blood.v98.10.3143.
51. Yamazaki, C., Sugiyama, M., Ohta, T., Hemmi, H., Hamada, E., Sasaki, I., Fukuda, Y., Yano, T., Nobuoka, M., Hirashima, T., et al. (2013). Critical roles of a dendritic cell subset expressing a chemokine receptor, XCR1. J. Immunol. *190*, 6071–6082. https://doi.org/10.4049/jimmunol.1202798.
52. Ugur, M., Kaminski, A., and Pabst, O. (2018). Lymph node gammadelta and alphabeta CD8(+) T cells share migratory properties. Sci. Rep. *8*, 8986. https://doi.org/10.1038/s41598-018-27339-8.
53. Kitano, M., Yamazaki, C., Takumi, A., Ikeno, T., Hemmi, H., Takahashi, N., Shimizu, K., Fraser, S.E., Hoshino, K., Kaisho, T., and Okada, T. (2016). Imaging of the cross-presenting dendritic cell subsets in the skin-draining lymph node. Proc. Natl. Acad. Sci. USA *113*, 1044–1049. https://doi.org/10.1073/pnas.1513607113.
54. Satpathy, A.T., Kc, W., Albring, J.C., Edelson, B.T., Kretzer, N.M., Bhattacharya, D., Murphy, T.L., and Murphy, K.M. (2012). Zbtb46 expression distinguishes classical dendritic cells and their committed progenitors from other immune lineages. J. Exp. Med. *209*, 1135–1152. https://doi.org/10.1084/jem.20120030.
55. Madisen, L., Zwingman, T.A., Sunkin, S.M., Oh, S.W., Zariwala, H.A., Gu, H., Ng, L.L., Palmiter, R.D., Hawrylycz, M.J., Jones, A.R., et al. (2010). A robust and high-throughput Cre reporting and characterization system for the whole mouse brain. Nat Neurosci *13*, 133–140. https://doi.org/10.1038/nn.2467.
56. Basak, O., Krieger, T.G., Muraro, M.J., Wiebrands, K., Stange, D.E., Frias-Aldeguer, J., Rivron, N.C., van de Wetering, M., van Es, J.H., van Oudenaarden, A., et al. (2018). Troy+ brain stem cells cycle through quiescence and regulate their number by sensing niche occupancy. Proc. Natl. Acad. Sci. USA *115*, E610–E619. https://doi.org/10.1073/pnas.1715911114.
57. Pircher, H., Bürki, K., Lang, R., Hengartner, H., and Zinkernagel, R.M. (1989). Tolerance induction in double specific T-cell receptor transgenic mice varies with antigen. Nature *342*, 559–561. https://doi.org/10.1038/342559a0.
58. Höpken, U.E., Droese, J., Li, J.-P., Joergensen, J., Breitfeld, D., Zerwes, H.-G., and Lipp, M. (2004). The chemokine receptor CCR7 controls lymph node-dependent cytotoxic T cell priming in alloimmune responses. Eur J Immunol *34*, 461–4700. https://doi.org/10.1002/eji.200324690.
59. Chen, E.Y., Tan, C.M., Kou, Y., Duan, Q., Wang, Z., Meirelles, G.V., Clark, N.R., and Ma'ayan, A. (2013). Enrichr: interactive and collaborative HTML5 gene list enrichment analysis tool. BMC Bioinformatics *14*, 128. https://doi.org/10.1186/1471-2105-14-128.

60. Kuleshov, M.V., Jones, M.R., Rouillard, A.D., Fernandez, N.F., Duan, Q., Wang, Z., Koplev, S., Jenkins, S.L., Jagodnik, K.M., Lachmann, A., et al. (2016). Enrichr: a comprehensive gene set enrichment analysis web server 2016 update. Nucleic Acids Res, 44. https://doi.org/10.1093/nar/gkw377.

61. Xie, Z., Bailey, A., Kuleshov, M.V., Clarke, D.J.B., Evangelista, J.E., Jenkins, S.L., Lachmann, A., Wojciechowicz, M.L., Kropiwnicki, E., Jagodnik, K.M., et al. (2021). Gene Set Knowledge Discovery with Enrichr. Curr Protoc, 1. https://doi.org/10.1002/cpz1.90.

62. Ritchie, M.E., Phipson, B., Wu, D., Hu, Y., Law, C.W., Shi, W., and Smyth, G.K. (2015). limma powers differential expression analyses for RNA-sequencing and microarray studies. Nucleic Acids Res *43*. https://doi.org/10.1093/nar/gkv007.

63. Thomas, P.D., Campbell, M.J., Kejariwa, A., Mi, H., Karlak, B., Daverman, R., Diemer, K., Muruganujan, A., and Narechania, A. (2003). PANTHER: a library of protein families and subfamilies indexed by function. Genome Res. *13*. https://doi.org/10.1101/gr.772403.

64. Stuart, T., Butler, A., Hoffman, P., Hafemeister, C., Papalexi, E., Mauck, W.M., 3rd, Hao, Y., Stoeckius, M., Smibert, P., and Satija, R. (2019). Comprehensive integration of single-cell data. Cell *177*, 1888–1902.e21. https://doi.org/10.1016/j.cell.2019.05.031.

65. Street, K., Risso, D., Fletcher, R.B., Das, D., Ngai, J., Yosef, N., Purdom, E., and Dudoit, S. (2018). Slingshot: cell lineage and pseudotime inference for single-cell transcriptomics. BMC Genomics *19*, 477. https://doi.org/10.1186/s12864-018-4772-0.

66. Colaprico, A., Silva, T.C., Olson, C., Garofano, L., Cava, C., Garolini, D., Sabedot, T.S., Malta, T.M., Pagnotta, S.M., Castiglioni, I., et al. (2016). TCGAbiolinks: an R/Bioconductor package for integrative analysis of TCGA data. Nucleic Acids Res, 44. https://doi.org/10.1093/nar/gkv1507.

67. Ogilvy, S., Metcalf, D., Gibson, L., Bath, M.L., Harris, A.W., and Adams, J.M. (1999). Promoter elements of vav drive transgene expression in vivo throughout the hematopoietic compartment. Blood *94*, 1855–1863.

68. Kastenmuller, W., Gasteiger, G., Gronau, J.H., Baier, R., Ljapoci, R., Busch, D.H., and Drexler, I. (2007). Cross-competition of CD8+ T cells shapes the immunodominance hierarchy during boost vaccination. J. Exp. Med. *204*, 2187–2198. https://doi.org/10.1084/jem.20070489.

69. Melsted, P., Booeshaghi, A.S., Liu, L., Gao, F., Lu, L., Min, K.H.J., da Veiga Beltrame, E., Hjörleifsson, K.E., Gehring, J., and Pachter, L. (2021). Modular, efficient and constant-memory single-cell RNA-seq preprocessing. Nat. Biotechnol. *39*, 813–818. https://doi.org/10.1038/s41587-021-00870-2.

STAR★METHODS

KEY RESOURCES TABLE

REAGENT or RESOURCE	SOURCE	IDENTIFIER
Antibodies		
Mouse anti-CCL21 (unconjugated)	Polyclonal, RnD Systems	Cat# AF457; RRID: AB_2072083
Rat anti-CD3 (APC-Fire 750-conjugated)	17A2, BioLegend	Cat# 100248; RRID: AB_2572118
Hamster anti-CD3ε (Biotin-conjugated)	145-2C11, eBioscience	Cat# 13-0031-82; RRID: AB_466319
Rat anti-CD4 (PE-conjugated)	OKT4, BioLegend	Cat# 317410; RRID: AB_571955
Rat anti-CD4 (Spark Near Infrared 685-conjugated)	GK1.5, BioLegend	Cat# 100476; RRID: AB_2819770
Rat anti-CD4 (Biotin-conjugated)	GK1.5, BioLegend	Cat# 100404; RRID: AB_312689
Mouse anti-CD8α (APC-conjugated)	3B5, Thermo Fisher Scientific	Cat# MHCD0805; RRID: AB_10392701
Rat anti-CD8α (Brilliant Violet 510-conjugated)	53-6.7, BioLegend	Cat# 100752; RRID: AB_2563057
Rat anti-CD8α (Brilliant Ultraviolet 805-conjugated)	53-6.7, BD Biosciences	Cat# 612898; RRID: AB_2870186
Rat anti-CD8β (Brilliant Violet 421-conjugated)	YTS156.7.7, BioLegend	Cat# 126629; RRID:
Rat anti-CD8β (*in vivo* depleting)	53-5.8, BioXCell	Cat# BE0223; RRID: AB_2687706
Rat anti-CD11b (Alexa Fluor 488-conjugated)	M1/70, BioLegend	Cat# 101217; RRID: AB_389305
Rat anti-CD11b (Alexa Fluor 647-conjugated)	M1/70, BioLegend	Cat# 101226; RRID: AB_830642
Rat anti-CD11b (Brilliant Violet 570-conjugated)	M1/70, BioLegend	Cat# 101233; RRID: AB_10896949
Rat anti-CD11b (Brilliant Violet 650-conjugated)	M1/70, BioLegend	Cat# 101259; RRID: AB_2566568
Rat anti-CD11b (PerCP Cy5.5-conjugated)	M1/70, BioLegend	Cat# 101228; RRID: AB_893232
Rat anti-CD11b (Spark Ultraviolet 387-conjugated)	M1/70, BioLegend	Cat# 101291; RRID: AB_2922453
Rat anti-CD11b (Biotin-conjugated)	M1/70, BioLegend	Cat# 101204; RRID: AB_312787
Hamster anti-CD11c (APC-conjugated)	N418, Thermo Scientific Fisher	Cat# 17-0114-82; RRID: AB_469346
Hamster anti-CD11c (Brilliant Violet 421-conjugated)	N418, BioLegend	Cat# 117330; RRID: AB_11219593
Hamster anti-CD11c (Brilliant Violet 711-conjugated)	N418, BioLegend	Cat# 117349; RRID: AB_2563905
Hamster anti-CD11c (Brilliant Ultraviolet 805-conjugated)	N418, BD Biosciences	Cat# 749038; RRID: AB_2873432
Hamster anti-CD11c (Biotin-conjugated)	N418, BioLegend	Cat# 117304; RRID: AB_313773
Rat anti-CD16/32 (Brilliant Ultraviolet 737-conjugated)	93, BD Biosciences	Cat# 751697; RRID: AB_2875682
Rat anti-CD19 (APC-Fire 750-conjugated)	6D5, BioLegend	Cat# 115558; RRID: AB_2572120
Rat anti-CD19 (Biotin-conjugated)	6D5, BioLegend	Cat# 115504; RRID: AB_313639
Rat anti-CD24 (eFluor 450-conjugated)	M1/69, Thermo Fisher Scientific	Cat# 48-0242-82; RRID: AB_1311169
Rat anti-CD26 (Brilliant Ultraviolet 563-conjugated)	H194-112, BD Biosciences	Cat# 741249; RRID: AB_2870799
Rat anti-CD31 (Alexa Fluor 488-conjugated)	MEC13.3, BioLegend	Cat# 102513; RRID: AB_493413
Rat anti-CD31 (Alexa Fluor 647-conjugated)	MEC13.3, BioLegend	Cat# 102516; RRID: AB_2161029

(*Continued on next page*)

Continued

REAGENT or RESOURCE	SOURCE	IDENTIFIER
Rat anti-CD31 (Alexa Fluor 700-conjugated)	390, BioLegend	Cat# 102444; RRID: AB_2832289
Rat anti-CD31 (Alexa Fluor 700-conjugated)	MEC13.3, Novus Biologicals	Cat# NB600-1475AF700; RRID: AB_789108
Rat anti-CD31 (Brilliant Violet 421-conjugated)	390, BioLegend	Cat# 102424; RRID: AB_2650892
Rat anti-CD31 (Brilliant Violet 480-conjugated)	MEC13.3, BD Biosciences	Cat# 565629; RRID: AB_2739310
Rat anti-CD34 (PE-conjugated)	RAM34, BD Biosciences	Cat# 551387; RRID: AB_394176
Rat anti-CD34 (eFluor 660-conjugated)	RAM34, Thermo Fisher Scientific	Cat# 50-0341-82; RRID: AB_10596826
Rat anti-CD34 (PE-Dazzle 594-conjugated)	SA376A4, BioLegend	Cat# 152210; RRID: AB_2734219
Rat anti-CD45R (Brilliant Violet 421-conjugated)	RA3-6B2, BioLegend	Cat# 103251; RRID: AB_2562905
Rat anti-CD45R (Brilliant Violet 480-conjugated)	RA3-6B2, BD Biosciences	Cat# 565631; RRID: AB_2739311
Rat anti-CD45R (PE-Cy7-conjugated)	RA3-6B2, BioLegend	Cat# 103222; RRID: AB_313005
Rat anti-CD45R (Spark Blue 550-conjugated)	RA3-6B2, BioLegend	Cat# 103266; RRID: AB_2832304
Rat anti-CD45R (Biotin-conjugated)	RA3-6B2, BioLegend	Cat# 103204; RRID: AB_312989
Mouse anti-CD45.1 (Brilliant Violet 650-conjugated)	A20, BioLegend	Cat# 110736; RRID: AB_2562564
Mouse anti-CD45.2 (Spark Near Infrared 685-conjugated)	104, BioLegend	Cat#109864; RRID: AB_2876424
Rat anti-CD62E (*in vivo* blocking)	10E9.6, BD Biosciences	Cat# 553749; RRID: AB_2186705
Rat anti-CD62L (*in vivo* blocking)	Mel-14, BioXCell	Cat# BE0021; RRID: AB_1107665
Rat anti-CD62P (*in vivo* blocking)	RB40.34, BD Biosciences	Cat#553742; RRID: AB_2254315
Mouse anti-CD64 (Brilliant Violet 421-conjugated)	X54-5/7.1, BioLegend	Cat# 139309; RRID: AB_2562694
Hamster anti-CD81 (PE-conjugated)	Eat-2, BioLegend	Cat# 104906; RRID: AB_2076266
Hamster anti-CD81 (PE-Cy7-conjugated)	Eat-2, BioLegend	Cat# 104914; RRID: AB_2810340
Rat anti-CD86 (Brilliant Ultraviolet 737-conjugated)	GL1, BD Biosciences	Cat# 741737; RRID: AB_2871107
Hamster anti-CD103 (Alexa Fluor 647-conjugated)	2E7, BioLegend	Cat# 121410; RRID: AB_535952
Hamster anti-CD103 (PerCP-eFluor 710-conjugated)	2E7, Thermo Fisher Scientific	Cat# 46-1031-82; RRID: AB_2573704
Rat anti-CD115 (Brilliant Blue 700-conjugated)	AFS98, BD Biosciences	Cat# 750887; RRID: AB_2874983
Rat anti-CD115 (Brilliant Ultraviolet 661-conjugated)	T38-320, BD Biosciences	Cat# 749973; RRID: AB_2874200
Rat anti-CD117 (Brilliant Violet 421-conjugated)	2B8, BioLegend	Cat# 105828; RRID: AB_11204256
Rat anti-CD117 (Brilliant Violet 605-conjugated)	2B8, BioLegend	Cat# 105847; RRID: AB_2783047
Rat anti-CD127 (PE-Dazzle 594-conjugated)	A7R34, BioLegend	Cat# 135032; RRID: AB_2564217
Rat anti-CD135 (APC-conjugated)	A2F10, BioLegend	Cat# 135310; RRID: AB_2107050
Rat anti-CD135 (PE-conjugated)	A2F10, BioLegend	Cat# 135305; RRID: AB_1877218
Rat anti-CD172a (Brilliant Violet 750-conjugated)	P84, BD Biosciences	Cat# 747007; RRID: AB_2871781

(*Continued on next page*)

Continued

REAGENT or RESOURCE	SOURCE	IDENTIFIER
Hamster anti-CD183 (Brilliant Ultraviolet 805-conjugated)	CXCR3-173, BD Biosciences	Cat# 748700; RRID: AB_2873104
Rat anti-CD197 (Alexa Fluor 647-conjugated)	4B12, BioLegend	Cat# 120109; RRID: AB_389235
Rat anti-CD197 (PE-conjugated)	4B12, BioLegend	Cat# 120105; RRID: AB_389357
Rat anti-CD205 (PE-Dazzle 594-conjugated)	NLDC-145, BioLegend	Cat# 138218; RRID: AB_2687398
Rat anti-CD226 (PE-Cy7-conjugated)	10E5, BioLegend	Cat# 128812; RRID: AB_2566629
Rat anti-CD370 (Brilliant Violet 480-conjugated)	10B4, BD Biosciences	Cat# 746743; RRID: AB_2744006
Mouse anti-CX3CR1 (APC-conjugated)	SA011F11, BioLegend	Cat# 149008; RRID: AB_2564492
Mouse anti-CX3CR1 (Brilliant Violet 421-conjugated)	SA011F11, BioLegend	Cat# 149023; RRID: AB_2565706
Mouse anti-CX3CR1 (Brilliant Violet 650-conjugated)	SA011F11, BioLegend	Cat# 149033; RRID: AB_2565999
Mouse anti-CX3CR1 (Brilliant Violet 785-conjugated)	SA011F11, BioLegend	Cat# 149029; RRID: AB_2565938
Rat anti-ER-TR7 (Alexa Fluor 405-conjugated)	ER-TR7, Novus Biologicals	Cat# NB100-64932AF405; RRID: AB_963381
Rat anti-ER-TR7 (Alexa Fluor 594-conjugated)	ER-TR7, Santa Cruz Biotechnology	Cat# sc-73355 AF594; RRID: AB_1122890
Rat anti-ER-TR7 (Alexa Fluor 700-conjugated)	ER-TR7, Novus Biologicals	Cat# NB100-64932AF700; RRID: AB_963381
Rat anti-ESAM (PE-Cy7-conjugated)	1G8/ESAM, BioLegend	Cat# 136212; RRID: AB_2860680
Rat anti-F4/80 (Brilliant Ultraviolet 395-conjugated)	T45-2342, BD Biosciences	Cat# 565614; RRID: AB_2739304
Rabbit anti-GFP (Alexa Fluor 488-conjugated)	Polyclonal, Thermo Fisher Scientific	Cat# A21311; RRID: AB_221477
Rat anti-Ki-67 (eFluor 450-conjugated)	SolA15, Thermo Fisher Scientific	Cat# 48-5698-82; RRID: AB_11149124
Rat anti-Ki-67 (eFluor 660-conjugated)	SolA15, Thermo Fisher Scientific	Cat# 50-5698-82; RRID: AB_2574235
Rat anti-Ly6A/E (Brilliant Ultraviolet 496-conjugated)	D7, BD Biosciences	Cat# 750169; RRID: AB_2874374
Rat anti-Ly6C (Alexa Fluor 488-conjugated)	HK1.4, BioLegend	Cat# 128022; RRID: AB_10639728
Rat anti-Ly6C (Brilliant Violet 785-conjugated)	HK1.4, BioLegend	Cat# 128041; RRID: AB_2565852
Mouse anti-Ly6C (eFluor 450-conjugated)	HK1.4, Thermo Fisher Scientific	Cat# 48-5932-82; RRID: AB_10805519
Rat anti-Ly6C/G (Brilliant Ultraviolet 395-conjugated)	RB6-8C5, BD Biosciences	Cat# 563849; RRID: AB_2738450
Rat anti-Ly6G (Spark Blue 550-conjugated)	1A8, BioLegend	Cat# 127663; RRID: 127663
Rat anti-Ly6G (Spark Near Infrared 685-conjugated)	1A8, BioLegend	Cat# 127607; RRID: 127607
Rat anti-Lyve1 (Alexa Fluor 488-conjugated)	ALY7, eBioscience	Cat# 53-0443-80; RRID: AB_1633415
Rat anti-Lyve1 (eFluor 660-conjugated)	ALY7, Thermo Fisher Scientific	Cat# 50-0443-82; RRID: AB_10597449
Rat anti-MHC-II (Alexa Fluor 488-conjugated)	M5/114.15.2, BioLegend	Cat# 107616; RRID: AB_493523
Rat anti-MHC-II (Alexa Fluor 700-conjugated)	M5/114.15.2, BioLegend	Cat# 107622; RRID: AB_493727

(*Continued on next page*)

Continued

REAGENT or RESOURCE	SOURCE	IDENTIFIER
Mouse anti-MHC-II (Brilliant Ultraviolet 395-conjugated)	25-9-17, BD Biosciences	Cat# 745580; RRID: AB_2743096
Mouse anti-NK1.1 (APC-Fire 750-conjugated)	PK136, BioLegend	Cat# 108752; RRID: AB_2629764
Mouse anti-NK1.1 (Biotin-conjugated)	PK136, BioLegend	Cat# 108704; RRID: AB_313391
Rat anti-PNAd (Alexa Fluor 594-conjugated)	MECA-79, BioLegend	Cat# 120805; RRID: AB_2650843
Rat anti-Siglec-H (Brilliant Blue 700-conjugated)	440c, BD Biosciences	Cat# 747668; RRID: AB_2744229
Hamster anti-TCR-β (APC-Fire 750-conjugated)	H57-597, BioLegend	Cat# 109246; RRID: AB_2629697
Rat anti-Ter119 (APC-Fire 750-conjugated)	TER-119, BioLegend	Cat# 116250; RRID: AB_2819833
Mouse anti-XCR1 (APC-conjugated)	ZET, BioLegend	Cat# 148206; RRID: AB_2563932
Mouse anti-XCR1 (Brilliant Violet 421-conjugated)	ZET, BioLegend	Cat# 148216; RRID: AB_2565230
Mouse anti-XCR1 (FITC-conjugated)	ZET, BioLegend	Cat# 148210; RRID: AB_2564366
Mouse anti-XCR1 (PE-conjugated)	ZET, BioLegend	Cat# 148204; RRID: AB_2563843
Chicken anti-Goat IgG (H+L) (Alexa Fluor 488-conjugated)	Polyclonal, Thermo Fisher Scientific	Cat# A21467; RRID: AB_2535870
TruStain FcX™ PLUS rat anti-CD16/32 (unconjugated)	S17011E, BioLegend	Cat# 156604; RRID: AB_2783138
TotalSeq™-A0301 anti-mouse Hashtag 1	M1/42; 30-F11; BioLegend	Cat# 155801; RRID: AB_2750032
TotalSeq™-A0302 anti-mouse Hashtag 2	M1/42; 30-F11; BioLegend	Cat# 155803; RRID: AB_2750033
TotalSeq™-A0303 anti-mouse Hashtag 3	M1/42; 30-F11; BioLegend	Cat# 155805; RRID: AB_2750034
TotalSeq™-A0304 anti-mouse Hashtag 4	M1/42; 30-F11; BioLegend	Cat# 155807; RRID: AB_2750035
Ultra-LEAF™ Purified rat isotype control	RTK2758, BioLegend	Cat# 400544; RRID: AB_11147167
Bacterial and virus strains		
Modified Vaccinia Ankara	Brewitz et al.[9]	N/A
Chemicals, peptides, and recombinant proteins		
ß-Mercaptoethanol	Gibco	Cat# 31350010
Agarose, Low Melting Point	Promega	Cat# V2111
Albumin from Bovine Serum (BSA) (Alexa Fluor 647-conjugated)	Thermo Fisher Scientific	Cat# A34785
Collagenase D	Sigma Aldrich	Cat# 11088882001
DNase I	Sigma Aldrich	Cat# DN25
Diphtheria Toxin	Sigma Aldrich	Cat# 322326-1MG
Fetal Bovine Serum	Sigma Aldrich	Cat# F7524-500ML
Fluoromount-G™ Mounting Medium	Invitrogen	Cat# 4958-02
FTY720	Sigma Aldrich	Cat# SML0700-25MG
Formalin solution, neutral buffered, 10%	Sigma Aldrich	Cat# HT501128-4L
Gelatin from cold water fish skin	Sigma Aldrich	Cat# G7041
Gilteritinib (ASP2215)	Selleckchem	Cat# S7754
Isoflurane CP 1ml/ml	CP Pharma	400806.00.00 Article # 1214
iTaq™ Universal SYBR® Green Supermix	Bio-Rad	Cat# 1725121
L-Lysine	Sigma Aldrich	Cat# L5501-100G
Molykote® High Vacuum Grease	DuPont	Cat# 4260145182276
MojoSort™ Buffer (5X)	BioLegend	Cat# 480017
MojoSort™ Streptavidin Nanobeads	BioLegend	Cat# 480016
Normal Mouse Serum	Invitrogen	Cat# 10410

(*Continued on next page*)

Continued

REAGENT or RESOURCE	SOURCE	IDENTIFIER
OCT freezing media	Sakura Finetek	Cat# 12351753
Optiprep™	Sigma Aldrich	Cat# D1556-250ML
Paraform-Aldehyde	Carl Roth	Cat# 0335.3
Penicillin-Streptomycin	Sigma Aldrich	Cat# P0781-100ML
RapiClear®	SunJin Lab	Cat# RC149001
Recombinant mouse IFN-α (carrier-free)	BioLegend	Cat# 752804
Recombinant mouse IFN-α	PBL Assay Science	Cat# 12100
Recombinant mouse FLT3L (carrier-free)	BioLegend	Cat# 550706
RPMI 1640, GlutaMAX Supplement	Gibco	Cat# 61870044
Sodium (meta)periodate	Sigma Aldrich	Cat# 769517-100G
Sucrose	Sigma-Aldrich	Cat#: 1.07687
Superfrost Plus object slides	VWR	Cat#: 631-0108
Tamoxifen	Sigma Aldrich	Cat# T5648-1G
TRIS Hydrochloride	Carl Roth	Cat# 9090.2
Triton-X 100	Carl Roth	Cat# 3051.2
UNC2025 HCl	Selleckchem	Cat# S7576
Veet Pure Hair Removal Cream	Veet	Cat# 310000091434
Critical commercial assays		
Chromium Single Cell 3' GEM, Library & Gel Bead Kit v3	10x Genomics	Cat# PN-1000075
iScript™ cDNA Synthesis Kit	Bio-Rad	Cat# 1708890
RNeasy Plus Micro Kit	QIAGEN	Cat# 74034
Zombie NIR™ Fixable Viability Kit	BioLegend	Cat# 423106
Zombie Aqua™ Fixable Viability Kit	BioLegend	Cat# 423102
Deposited data		
Raw and processed mouse scRNA-sequencing data	This paper	GEO: GSE204815
Experimental models: Cell lines		
UMNSAH/DF-1	Himly et al.[49]	RRID: CVCL_0570
Experimental models: Organisms/strains		
Mouse: C57BL/6J	Janvier	RRID: IMSR_JAX:000664
Mouse: CD45.1 (B6.SJL-Ptprca Pepcb/BoyJ)	Janowska-Wieczorek et al.[50]	RRID: IMSR_JAX:002014
Mouse: Xcr1Venus (Xcr1tm2(HBEGF/Venus)Ksho)	Yamazaki et al.[51]	N/A
Mouse: Xcr1DTR (Xcr1tm1Ksho)	Yamazaki et al.[51]	N/A
Mouse: Dendra2-VHD (B6.tg(HD2)	Ugur et al.[52]	N/A
Mouse: Xcr1KikGR (B6.Cg-Xcr1<tm3(KikGR)Ksho>)	Kitano et al.[53]	N/A
Mouse: Zbtb46GFP (B6.129S6(C)-Zbtb46tm1.1Kmm/J)	Satpathy et al.[54]	RRID: IMSR_JAX:027618
Mouse: Rosa26LSLtdTomato (B6.Cg-Gt(ROSA)26Sortm9 (CAG-tdTomato)Hze/J)	Madisen et al.[55]	RRID: IMSR_JAX:007909
Mouse: Mki67CreERT2 (Mki67tm2.1(cre/ERT2)Cle/J)	Basak et al.[56]	RRID: IMSR_JAX:029803
Mouse: P14-TCR-transgenic (B6. Tg(TcrLCMV)327Sdz/TacMmjax)	Pircher et al.[57]	RRID: MMRRC_037394-JAX
Mouse: CCR7-/- (B6.129P2(C)-Ccr7tm1Rfor/J)	Höpken et al.[58]	RRID: IMSR_JAX:006621

(*Continued on next page*)

Continued

REAGENT or RESOURCE	SOURCE	IDENTIFIER
Mouse: Prtn3CreERT2-hCD4	This paper; Generated in cooperation with Ozgene	N/A
Software and algorithms		
Adobe After Effects	Adobe	https://www.adobe.com/de/products/aftereffects
Adobe Illustrator	Adobe	RRID:SCR_010279
Attune NxT Software	Thermo Fisher Scientific	RRID:SCR_019590
BD FACSDiva Software	BD Biosciences	RRID:SCR_001456
Biorender	Biorender	RRID:SCR_018361
Cell Render	10x Genomics	RRID:SCR_017344
EnrichR	Chen et al.[59]; Kuleshov et al.[60]; Xie et al.[61]	RRID:SCR_001575 https://maayanlab.cloud/Enrichr/
Flowjo v10	BD Biosciences	RRID:SCR_008520
GNU Image Manipulation Program	GIMP	RRID:SCR_003182
GraphPad Prism	GraphPad	RRID:SCR_002798
Imaris v8.3	Bitplane	RRID:SCR_007370
Leica Las X	Leica	RRID:SCR_013673
limma	Ritchie et al.[62]	RRID:SCR_010943
Microsoft Excel	Microsoft	RRID:SCR_016137
PANTHER	Thomas et al.[63]	RRID:SCR_004869
Seurat	Stuart et al.[64]	RRID:SCR_007322
Slingshot	Street et al.[65]	RRID:SCR_017012
SoftMax Pro GxP Software	Molecular Devices	https://www.moleculardevices.com/products/microplate-readers/acquisition-and-analysis-software/softmax-pro-gxp-software
SpectroFlo	Cytek	https://cytekbio.com/pages/spectro-flo
TCGAbiolinks	Colaprico et al.[66]	RRID:SCR_017683

RESOURCE AVAILABILITY

Lead contact

Further information and requests for resources and reagents should be directed to and will be fulfilled by lead contact, Wolfgang Kastenmüller, (wolfgang.kastenmueller@uni-wuerzburg.de).

Materials availability

Prtn3$^{CreERT2\text{-}hCD4}$ mouse line was generated in this study and is available from the lead contact upon request.

Data and code availability

- Single cell RNA sequencing data have been deposited at GEO and are publicly available as of the date of publication. Accession number is listed in the key resources table.
- This paper does not report original code.
- Any additional information required to reanalyze the data reported in this paper is available from the lead contact upon request.

EXPERIMENTAL MODEL AND SUBJECT DETAILS

Mice

Wild type (WT, C57BL.6, Jax#000664), WT CD45.1 (B6.SJL-Ptprca Pepcb/BoyJ , Jax#002014), *Xcr1*^{Venus} (Xcr1tm2(HBEGF/Venus)Ksho),[51] *Xcr1*^{DTR} (Xcr1tm1Ksho),[51] Dendra2-VHD (B6.tg(HD2),[52] *Xcr1*^{KikGR} (B6.Cg-Xcr1<tm3(KikGR)Ksho>),[53] *Zbtb46*^{GFP} (B6.129S6(C)-Zbtb46tm1.1Kmm/J, Jax#027618),[54] *Rosa26*^{LSLtdTomato} (B6.Cg-Gt(ROSA)26Sortm9(CAG-tdTomato)Hze/J, Jax#007909), *Mki67*^{CreERT2} (Mki67tm2.1(cre/ERT2)Cle/J, Jax#029803),[56] P14-TCR-transgenic (B6. Tg(TcrLCMV)327Sdz/TacMmjax, Jax#037394)[57] and *Prtn3*$^{CreERT2\text{-}hCD4}$ mice and WT mice were bred in house or purchased from Janvier Laboratories. Ccr7$^{-/-}$ (B6.129P2(C)-Ccr7tm1Rfor/J, Jax#006621) bone marrow was a kind gift from R. Förster from Hannover Medical School.

Prtn3$^{CreERT2\text{-}hCD4}$ mice were generated by Ozgene (Perth, Australia). Briefly, an IRES-CreERT2-IRES-humanCD4-FRT-neo-FRT construct was inserted into the 5th exon of the endogenous *Prtn3* gene after the endogenous stop codon. Neomycin cassette used for selection was then removed by the flippase enzyme. Human CD4 coding sequence used in the construct lacks the C-terminal 33 amino acids and contains the F43I mutation, generating a mutated and truncated protein that precludes signaling and association with MHCII.[67]

All mice used in this project were 6–30 weeks old and maintained in specific-pathogen-free conditions at an Association for Assessment and Accreditation of Laboratory Animal Care-accredited animal facility. All procedures were approved by the Lower Franconia Government. All mouse strains are published (except *Prtn3*$^{CreERT2\text{-}hCD4}$) and were either generated or later backcrossed to a C57BL/6 genetic background.

Virus production

MVA-WT viral stocks were produced with DF-1 cells as previously described.[68] Infected cells were incubated for 48-72 h at 37°C, 5% CO2 before harvest. After harvest, cells were homogenized and supernatant containing the virus was purified over a sucrose cushion. Viral titers were determined by infecting DF-1 cells with dilution series of the viral stocks.

METHOD DETAILS

Infection and treatment of mice

For depletion of CD8β$^+$ T cells, 100 μg anti-CD8β antibody (53-5.8, BioXCell) was injected intraperitoneally (i.p.) 5 days before analysis. For *in vivo* antibody labelling, 5 μg anti XCR1_PE antibody (ZET, BioLegend) was injected intravenously (i.v.) 1 hour before analysis. Left inguinal, brachial and axillary LNs were pooled for flow cytometry analysis while their right counterparts were fixed for confocal microscopy. For intravital microscopy and analysis of some vibratome slices with confocal microscopy, 1 μg anti CD34_PE antibody (RAM34, BD) was injected intravenously (i.v.) before analysis to visualize blood vessels. For the antigen uptake assays, 10 μg (experiment in Figure 1G) or 1 μg (experiment in Figure 6G) bovine serum albumin conjugated with Alexa Fluor 647 (Invitrogen) in 30 μL PBS was injected subcutaneously (s.c.) into the foot hock 2 hours before analysis. Both left and right draining LNs were pooled for analysis. For depletion of XCR1$^+$ cDC1, mice were injected i.p. 1 μg of diphtheria toxin (DTx) (Sigma Aldrich) once or twice. For repopulation time points after depletion, days were counted from the last DTx injection if two injections were performed. For inducing CreERT2 recombinase activity, mice were injected i.p. 3 mg Tamoxifen (Sigma Aldrich) dissolved in corn oil (Sigma Aldrich). For MVA infection, 2x10^7 IU of MVA-WT in 30 μL PBS was injected s.c. into the foot hock. For interferon-alpha (IFNα) treatments, 100 U (PBL Assay Science) or 25-50 ng (BioLegend) in 30 μL PBS was injected s.c. into the foot hock. For Flt3L treatments, mice were injected for systemic treatment i.p. with 10 μg or for local treatments s.c. in the foot hock with 1μg of recombinant mouse Flt3L (BioLegend) in PBS. For CD62L blockade, mice were injected i.p. with 250 μg anti-CD62L (MEL-14, BioLegend) or isotype (RTK2758, BioLegend) antibody. For CD62E/CD62P blockade, mice were injected i.v. with a mixture of 50 μg anti-CD62E (10E9.6, BD) and 50 μg anti-CD62P (P84, BD) or 100 μg isotype (RTK2758, BioLegend) antibody. For S1P blockade, mice were injected i.p. with 25 μg FTY720 (Sigma Aldrich). For Flt3 inhibition, mice were injected i.p. with 3 mg/kg UNC2025 HCl (Selleckchem.com) together with p.o. 10 mg/kg Gilteritinib (Selleckchem.com).

In vivo photoconversion

Photoconversion of inguinal LNs (iLNs) of 6 weeks-old *Xcr1*^{KikGR} mice were performed as previously described[52] with some modifications. Mice were anesthetized with a mixture of Air/O_2/Isoflurane (CP-Pharma) and their flanks over the iLNs were shaved and cleaned with depilatory cream (Veet). iLNs were identified and illuminated through the skin with a custom-made collimated light source (Prizmatix, Mountain Photonics) equipped with 405 nm Silver-LED and 400 nm long-pass filter at maximum intensity for 60 seconds two times from a distance of ~1 cm. During the illuminations, the skin was kept wet with PBS and area outside of the iLN were covered with aluminium foil to avoid undesired photoconversion. Mice were allowed to wake up and sacrificed at indicated time points after photoconversion.

Ex vivo photoconversion

Fresh LNs from unmanipulated Dendra2-VHD mice were embedded in 2% low melting agarose (Promega) in PBS solution that was kept at 25°C and placed on ice after embedding for solidification of the agarose. Agarose blocks were then cut into 200 μm slices using a vibratome (Leica) while kept in cold PBS. Slices were then placed on coverslips with PBS and LN paracortex regions were identified with confocal microscopy based on autofluorescence, immune cell density and Dendra2 brightness differences between B and T cells. A square area in the paracortex was selected with 0.75 zoom and 7-9 z-stacks of 3 μm were photoconverted with 50% power of the 405 nm laser at a scan speed of 100 lines per second. After photoconversion, 8-10 converted or unconverted control LN slices were pooled, digested and stained for flow cytometry analysis as described in the "LN digestion" and "flow cytometry" sections.

Isolation of BM cells

BM cells were isolated via centrifugation. Tibia and femur of the indicated mice were cut from one end and placed into a 0.5 mL tube with a hole at the bottom and this tube was placed into a 1.5 mL tube. This assembly was centrifuged at 5000 rpm in a standard

table-top centrifuge for 30 seconds. Resulting pellet was resuspended in PBS and red blood cell lysis was performed with Ammonium-Chloride-Potassium (ACK) buffer.

BM reconstitution

Mice were lethally irradiated with 9 Gy using a Faxitron CP160 (Faxitron Bioptics) and 5-10x10^6 donor BM cells were i.v. injected into irradiated recipients 6h after irradiation. For WT:Ccr7$^{-/-}$ mixed chimeras cells BM cells were mixed at a 85:15 ratio and for *Xcr1*^{DTR}:*Xcr1*^{Venus} mixed chimeras cells were mixed at a 50:50 ratio. Mice were analyzed $\geq$6 weeks after irradiation.

LN digestion

LNs were digested using RPMI 1640 GlutaMAX medium (Gibco) supplemented with 2% fetal calf serum (FCS), penicillin-streptomycin (100 U/mL, Sigma-Aldrich), Collagenase D (3 mg/mL, Roche) and DNase I (20 μg/mL, Sigma Aldrich). Before digestions, LNs were cut into small pieces for at least 1 minute using sharp-end scissors. When digesting 6 LNs (inguinal, brachial and axillary), they were incubated in 800 μL digestion medium for 5-10 minutes in a thermo-shaker (Grant-Bio) at 37°C with 300 rpm shaking. After this first digestion, the LN pieces were mixed well with a micropipette for at least 30 seconds and big pieces were let to sediment for 1-2 minutes. Then, 700-750 μL supernatant was collected and mixed with 8 mL of PBS with 2% FCS and kept on ice. 750 μL of fresh digestion medium was added to the remaining pieces and incubated 15-20 minutes in a thermo-shaker at 37°C with 300 rpm shaking. After this second digest, the suspension was mixed well with a micropipette for at least 1 minute and all of the suspension was collected and combined with the first digestion part. When digesting only 1-2 LNs, they were incubated in 400 μL digestion medium for 15-20 minutes in a thermo-shaker at 37°C with 300 rpm shaking. After this digestion, the LN pieces were mixed well with a micropipette for at least 1 minute and all of the suspension was collected and mixed with 8 mL of PBS with 2% FCS. After the digestions, cells were centrifuged and resuspended in PBS with 2% FCS.

Flow cytometry

Cell suspensions were stained for flow cytometry analysis in PBS with 2% FCS in 96-well U- or V-bottom plates. Cell numbers used for stainings were adjusted so that in each experiment similar number of cells were stained for all groups. First, samples were centrifuged and resuspended in 100 μL Zombie NIR or Zombie Aqua Live/Dead dye (1:400, BioLegend) in PBS and incubated for 10-15 minutes on ice. After the incubation, 100 μL PBS with 2% FCS added on to the cell suspensions and centrifuged. Then cells were resuspended in 50 μL TruStain FcX PLUS (1:1000, BioLegend) for blocking and incubated on ice for 5-10 minutes. After blocking, 50 μL of double-concentrated antibody mixture was added on top and incubated for 20-25 minutes on ice. Then cells were washed twice with PBS with 2% FCS, resuspended in PBS with 2% FCS and analyzed at Attune NxT (Thermo Fischer Scientific) or Cytek Aurora 5-Laser (Cytek Biosciences). Appropriate flurorescent-dye-conjugated combinations of the following antibodies were used (BioLegend, BD Biosciences or eBioscience): anti-mouse CD19 (6D5), CD3 (17A2), TCRβ (H57-597), NK1.1 (PK136), Ter119 (TER-119), Ly6C (HK1.4), B220 (RA3-6B2), Siglec-H (551), CX3CR1 (SA011F11), CD11c (N418), MHCII (M5/114.15.2), CD26 (H194-112), CD24 (M1/69), CD172a (P84), CD11b (M1/70), CD117 (2B8), CD135 (A2F10), XCR1 (ZET), CD4 (GK1.5), CD115 (T38-320 or AFS98), Esam (1G8/ESAM), CD8α (53-6.7), CD205 (NLDC-145), CD81 (Eat-2), CD86 (GL1), CD103 (2E7), Ly6A/E (D7), CD226 (10E5), Ly6G (1A8), Gr-1 (RB6-8C5), CD16/32 (93), CD34 (RAM34) CD45.2 (104), CD45.1 (A20) and anti-human CD4 (OKT4). For the multidimensional tSNE analysis of repopulating cDC1, markers CD24, XCR1, CD8α, CD205, CD103, CD26, CD81, CD86, CD4, Esam, Ly6A/E, CD117 and CX3CR1 were used. For the multidimensional tSNE analysis of MHCII$^-$ preDC, markers Ly6A/E, CD115, CD24, CD8α, CD11b, CD117, CX3CR1, Ly6C, XCR1, Siglec-H, CD81, Esam and CD4 were used. FlowJo (BD Biosciences) software was used for the analysis.

Cell enrichment and sorting

For the scRNAseq analysis of preDC, digested LN cell suspensions were enriched before sorting by using biotin-conjugated anti-CD3, anti-CD19, anti-B220 and anti-NK1.1 antibodies and streptavidin Mojo magnetic beads (BioLegend) according to the manufacturer's instructions. After enrichment, cells were stained with Zombie NIR (BioLegend), Streptavidin, antibodies against CD3, CD19, NK1.1, Ly6G, CD11b, B220, CD11c, MHCII and CD135 with appropriate fluorochromes and sorted as Zombie$^-$CD3$^-$CD19$^-$NK1.1$^-$Ly6G$^-$B220$^-$CD11c$^+$MHCII$^-$CD11b$^{-/lo}$ CD135$^+$ cells with FACSAria III (BD Biosciences).

For preDC transfer, BM cells were enriched before sorting by using biotin-conjugated anti-CD3, anti-CD19, anti-B220 and anti-Ly6G antibodies and streptavidin Mojo magnetic beads (BioLegend) according to the manufacturer's instructions. After enrichment, cells were stained with Zombie NIR (BioLegend), Streptavidin, antibodies against CD3, CD19, TCRβ, NK1.1, Ly6G, B220, CD11c and CD135 with appropriate fluorochromes and sorted as Zombie$^-$CD3$^-$CD19$^-$TCRβ$^-$NK1.1$^-$GFP$^+$Ly6G$^-$ B220$^-$ CD11c$^+$ CD135$^+$ cells with FACSAria III (BD Biosciences). For flow cytometry analysis 1x10^5, for histological analysis 2x10^5-3x10^5 GFP$^+$ preDC were transferred i.v. into recipients.

For T cell transfer, LN cells were enriched by using biotin-conjugated anti-CD19, anti-B220, anti-CD4, anti-CD11b, anti-CD4, anti-NK1.1 and anti-CD11c antibodies and streptavidin Mojo magnetic beads (BioLegend) according to the manufacturer's instructions. 1.5x10^6-2x10^6 Tomato$^+$CD8$^+$ P14 T cells were transferred i.v. into recipients.

Confocal microscopy

LNs were isolated and fixed in PLP buffer (0.05 M phosphate buffer containing 0.1 M L-lysine (pH 7.4), 2 mg/ml NaIO4 and 10 mg/ml paraformaldehyde) overnight at 4°C. Samples were dehydrated with 30% sucrose for 8 hours at 4°C, embedded in OCT freezing media (Sakura Finetek) and stored at -80°C. Serial 30 mm sections were cut on a CM3050S cryostat (Leica) and adhered to Superfrost Plus object slides (VWR). After rehydration with PBS for 5-10 minutes at room temeperature, sections were permeabilized and blocked with 0.1 M Tris containing 1% FCS (Sigma-Aldrich), 1% GCWFS (Sigma Aldrich), 0.3% Triton-X 100 (Carl Roth) and 1% normal mouse serum (Life Technologies) for 30 min at room temperature. Antibody stainings were performed in blocking buffer at 4°C overnight. Sections were washed with PBS and mounted with Fluoromount-G (eBioscience). For histological analysis of vibratome slices, fixed LNs were were embedded in 2% low melting agarose (Promega) in PBS solution that was kept at 25°C and placed on ice after embedding for solidification of the agarose. Agarose blocks were then cut into 200 μm slices using a vibratome (Leica) while kept in cold PBS. Then LN slices were stained with antibodies in blocking buffer overnight at 4°C in a 96-well plate and washed twice with PBS. After washing, LN slices were cleared for 24 hours using RapiClear (Sunjin Lab) at 4°C in a 96-well plate and embedded in RapiClear solution. Acquisition was performed on a Leica SP8 confocal microscope with LasX software. Appropriate flurorescent-dye-conjugated combinations of the following antibodies were used (BioLegend, BD Biosciences or eBioscience): CD8α (53-6.7), CD31 (MEC13.3), ER-TR7 (ER-TR7), CD34 (RAM34), B220 (RA3-6B2), CD8β (YTS156.7.7), Ki67 (SolA15), CD11b (M1/70), CD11c (N418), Lyve1 (ALY7), PNAd (MECA-79), CCL21 (MAB457) and anti-GFP (polyclonal).

Confocal microscopy image quantification

Confocal images were imported into Imaris (v8.3, Bitplane). To generate co-localized channels, semi-automatic 'surface' function was used and channels were masked based this surface. These masked- channels are shown with a subscript in the figures. To calculate cell localizations, semi-automatic 'spot' function was used. For preDC transfer analysis, transferred preDC were identified manually based on surrounding CD11c staining, size, GFP intensity and lack of autofluorescence. Intensity values of the channels (mean voxel fluorescence) and xyz coordinates of the spots were then exported to Excel (Microsoft), organized and coverted into .csv files. Csv files were then imported into FlowJo (BD Biosciences) for conversion into .fcs files and downstream analysis. Artificial spots were also created manually to delineate LN borders and the paracortex region. Paracortex region was identified using combinations of CD8β, ER-TR7, B220, CD31 and CD11b stainings, GFP and autofluorescence. Frequency of cells in LN regions was calculated by creating a gate using the manually created artificial spots. In the figure color descriptions, subscripts indicate masked channels and superscripts indicate relevant promoters or Cre-mediated recombinations. Except for preDC transfer, in all experiments only one section per LN and 1-4 LNs were analyzed per mouse. For preDC transfer, 25-30 sections per LN and 5-6 LNs were analyzed due to low number of detected preDC.

Intravital microscopy

Mice were anesthetized with isoflurane (CP-Pharma; 2% for induction, 1∼1.5% for maintenance, vaporized in an 80:20 mixture of O2 and air), inguinal LNs were exposed and intravital microscopy was performed. The imaging system was composed of Chameleon Ultra II Ti:Sapphire femtosecond pulsed (Coherent) laser tuned to 950nm, Onefive ORIGAMI 10 XPS femtosecond pulsed (NKT Photonics) laser tuned to 1055nm, Leica SP8 Dive Multiphoton upright microscope equipped with a 25× water immersion lens (NA = 1.0, Leica) and LAS X Life Science Platform software. The microscope was enclosed in an environmental chamber in which anesthetized mice were warmed by 36°C air and the surgically-exposed LN was kept at 36-37°C with warmed PBS. For dynamic imaging we typically used a z-stack of 100-150 μm and 3μm step size and acquired every 1min. Raw imaging data were processed and analyzed and processed with Imaris (Bitplane) and Adobe AfterEffect (Adobe). Supplemental movies created from the image stacks are at adjusted intensity projections and play at 300x real time.

Quantitative PCR

Inguinal and popliteal LNs were collected and homogenised using a TissueLyser II (QIAGEN), after which RNA was extracted from tissue homogenates using the RNeasy Plus Micro kit (QIAGEN), as per the manufacturer's instructions. Complementary DNA was synthesised from the resulting RNA with the iScript cDNA Synthesis kit (Bio-Rad), in accordance with the manufacturer's instructions. Expression of *Flt3l* mRNA was measured in cDNA on the CFX Connect Real-Time System (Bio-Rad) using the iTaq Universal SYBR Green Supermix (Bio-Rad) using primers *Flt3l* forward (5′-GGGAACCAAAACAAGGAACAAG-3′), *Flt3l* reverse (5′-GTCCATCGCCA TACCCAGA-3′), *Actb* forward (5′-CGACAACGGCTCCGGCATGT -3′) and *Actb* reverse (5′-CTAGGGCGGCCCACGATGGA -3′). *Flt3l* expression was normalised according to *Actb* expression based on the $2^{-\Delta\Delta Ct}$ method.

Hashtagging for scRNA sequencing

To combine different treatments and timepoints for scRNA sequencing, single cell suspensions from LNs were generated and together with the antibody mix for sorting, a specific TotalSeq™ Antibody mix (BioLegend) was added and incubated for 30 minutes at 4°C.

scRNA sequencing

Single-cells were sorted from sdLN using a FACSAria III (BD Biosciences), before being encapsulated into droplets with the ChromiumTM Controller (10x Genomics) and processed following manufacturer's specifications. Transcripts captured in all the cells

encapsulated with a bead were uniquely barcoded using a combination of a 16 bp 10x Barcode and a 10 bp unique molecular identifier (UMI). cDNA libraries were generated using the Chromium™ Single Cell 3' Library & Gel Bead Kit v3 (10x Genomics) following the detailed protocol provided by the manufacturer. Libraries were quantified by QubitTM 3.0 Fluometer (ThermoFisher) and quality was checked using 2100 Bioanalyzer with High Sensitivity DNA kit (Agilent). Libraries were sequenced with the NovaSeq 6000 platform (S1 Cartridge, Illumina) in 50 bp paired-end mode. The hashtag library was demultiplexed using CellRanger software (version 2.0.2). The gene expression library was demultiplexed and pseudo-aligned using kallisto and bustools,[69] discriminating between spliced and unspliced transcripts. Aligned spliced reads were used to quantify the expression level of mouse genes and generation of gene-barcode matrix. Subsequent data analysis was performed using Seurat R package (version 3.2).[64]

scRNA sequencing analysis

Quality control was performed, and viable cells were selected by excluding cells with UMI counts lower than 800 and above 4500, as well as cells having more than 5% of mitochondrial transcripts and more than 22000 transcripts in total. The contribution of cell cycle genes to the clustering was regressed out with the CellCycleScoring and ScaleData function of Seurat.[64] 2000 most variable genes used for the anchoring process were used for downstream analysis to calculate principal components, after log-normalization and scaling. Principle component analysis (PCA) was used for dimensionality reduction and to visualize a uniform manifold approximation and projection (UMAP) of the identified clusters. Contaminating cells and clusters were removed from the analysis based on marker genes *Cd3e*, *Cd3g*, *Trc1*, *Trbc2*, *Mafb* and *Nkg7*. P-values comparing gene expression of clusters and samples were calculated with the FindMarker function in Seurat. Gene list for Table S1 was generated using an adjusted p-value cutoff <0.05 and expression in the indicated cluster cutoff >50%.

Sample demultiplexing

Samples were demultiplexed with the HTODemux function integrated in Seurat with standard settings.

Trajectory analysis with Slingshot

Trajectories were predicted using Slingshot 1.4.0 package, using function slingshot with standard settings and starting cluster 5.[65] The isolated cDC1 lineage was analyzed for sample contribution to each cluster associated with the lineage. The number of cells from each sample was normalized across samples and afterwards the relative frequency of cluster contribution was calculated.

Gene ontology analysis

Genes associated with the pseudotime of the cDC1 lineage were identified by random forest calculation and selected for positive correlation. This gene list was analyzed using PANTHER Classification System (http://www.pantherdb.org) for enriched gene ontology terms and biological processes (PANTHER Overrepresentation Test (Released 20220202), reference list: *Mus musculus*, Fisher's exact test with false discovery rate correction).

QUANTIFICATION AND STATISTICAL ANALYSIS

Apart from the genomic data, all the biological data were analyzed using Prism 9 software (GraphPad) by two-tailed paired Student's t-test if the matching data points for compared groups are linked with lines, two-tailed unpaired Student's t-test if the matching data points for compared groups are not linked with lines or one-way ANOVA test if 3 or more groups were compared. All data are presented as mean±SD unless indicated in the figure legends.